

Minerals of the rhönite-kuratite series in paralavas from a new combustion metamorphic complex in the Choir–Nyalga basin (Central Mongolia): composition, mineral assemblages and formation conditions

IGOR S. PERETYAZHKO^{1,*}, ELENA A. SAVINA¹ AND ELENA A. KHROMOVA²

¹ Vinogradov Institute of Geochemistry, Siberian Branch of the Russian Academy of Sciences, 1a Favorsky str., Irkutsk 664033, Russia

² Geological Institute, Siberian Branch of the Russian Academy of Sciences, 6a Sakhyanova str., Ulan-Ude 670047, Russia

[Received 16 May 2016; Accepted 05 September 2016; Associate Editor: Stuart Mills]

ABSTRACT

This is the first description of rare minerals found in paralavas from a recently discovered combustion metamorphic complex in the Choir–Nyalga basin, Central Mongolia. The identified minerals contain strongly variable concentrations of Si, Ti, Mg, Fe²⁺ and Fe³⁺ and most commonly have compositions intermediate in a series from kuratite Ca₄Fe₁₀²⁺Ti₂O₄[Si₈Al₄O₃₆] and rhönite Ca₄(MgFe²⁺)₈Fe₂³⁺Ti₂O₄[Si₆Al₆O₃₆] to low-Ti kuratite and unnamed Ti-free Fe²⁺-analogue of rhönite Ca₄Fe₈²⁺Fe₄³⁺O₄[Si₈Al₄O₃₆]. The minerals crystallized in residual Si–Al–K and Si–Al–Ca–Fe immiscible melts after spinel, anorthite–bytownite, melilite, Al-clinopyroxene ± Mg–Fe olivine, together with Fe³⁺-bearing hercynite, Ca-rich fayalite, kirschsteinite, pyrrhotite ± native iron, wüstite, magnetite, celsian, hyalophane, Ba-orthoclase and fresnoite, but before nepheline ± kalsilite, and later sulfates, carbonates, an unidentified ‘X-mineral’ close to Al- and Fe-rich tobermorite and goethite. Micro-Raman spectroscopy of kuratite shows five bands near 133–155 (strong), 399–401, 545–566, 684–693 (strongest) and 828–839 cm⁻¹.

The kuratite-bearing Nyalga paralavas have bulk compositions with MgO/(MgO+FeO+Fe₂O₃), mol.% ~0.5 and a CIPW normative ratio of Ne/(Ne+Lc)=0.23–0.76. Minerals of the rhönite–kuratite series formed during paralava crystallization at ~1100°C. The diversity of the paralava mineral assemblages might result from local composition variations of Ca-rich silica-undersaturated melts derived from Fe-bearing carbonate-silicate sediments which were affected by nearby coal combustion sources at reducing conditions (IW–WM–QFM buffers) and at a nearly atmospheric pressure.

KEYWORDS: kuratite, rhönite–kuratite series, low-Ti kuratite, Ti-free Fe²⁺-analogue of rhönite, paralava, Nyalga combustion metamorphic complex, Choir–Nyalga basin, Central Mongolia.

Introduction

THE sapphirine supergroup includes sapphirine and surinamite groups or polysomatic series of minerals (Grew *et al.*, 2008). The sapphirine polysomatic series, in turn, is divided into sapphirine,

aenigmatite and rhönite subgroups according to the occupancy of the two largest octahedral *M* sites cations Mg, Na or Ca. The rhönite subgroup comprises several end-members in the classification scheme of Grew *et al.* (2008): rhönite Ca₄Mg₈Fe₂³⁺Ti₂O₄[Si₆Al₆O₃₆], dorrite Ca₄Mg₃Fe₉³⁺O₄[Si₃Al₈Fe₃³⁺O₃₆], serendibite Ca₄Mg₆Al₆O₄[Si₆B₃Al₃O₃₆], högtuvaite Ca₄Fe₆²⁺Fe₆³⁺O₄[Si₈Be₂Al₂O₃₆], makarochkinite Ca₄Fe₈²⁺Fe₂³⁺Ti₂O₄[Si₈Be₂Al₂O₃₆], welshite Ca₄Mg₉Sb₃⁵⁺O₄

*E-mail: pgmigor@mail.ru

<https://doi.org/10.1180/minmag.2016.080.144>

[Si₆Be₃AlFe³⁺₂O₃₆], the unnamed Ti³⁺-bearing Mg-analogue of rhönite Ca₄Mg₇AlTi³⁺Ti⁴⁺O₄ [Si₅Al₇O₃₆] and the unnamed Fe²⁺-analogue of rhönite. A mineral compositionally proximal to the end-member Fe²⁺-analogue of rhönite has been discovered in the D'Orbigny angrite (achondritic meteorite) from Argentina and approved by the International Mineralogical Association Commission on New Minerals, Nomenclature and Classification as kuratite Ca₄Fe²⁺₁₀Ti₂O₄[Si₈Al₄O₃₆] (IMA 2013-109). Recently four new minerals of the rhönite subgroup have been also approved: warkite (IMA 2013-129; Ma *et al.*, 2014) Ca₄Sc₁₂O₄[Al₁₂O₃₆], khesinite (IMA 2014-033; Galuskina *et al.*, 2014) Ca₄Mg₃Fe³⁺₉O₄[Si₃Fe³⁺₉O₃₆], beckettite (IMA 2015-001; Ma *et al.*, 2015) Ca₄V₁₂O₄[Al₁₂O₃₆] and addibischoffite (IMA 2015-006; Ma and Krot, 2015) Ca₄Al₁₂O₄[Al₁₂O₃₆]. The rhönite-subgroup minerals are very diverse in composition but most of them are Mg-Fe varieties (rhönite and dorrite–khesinite series) with the parameter $X_{\text{Mg}} = \text{Mg}/(\text{Mg} + \text{Fe}^{2+}) > 0.5$ (in atoms per formula unit, apfu). Minerals with $X_{\text{Mg}} < 0.5$, similar to kuratite, as well as other varieties enriched in B, Be, Ti³⁺, Sb, Sc, V and Al are of extremely rare natural occurrence.

Rhönite occurs as phenocrysts, microphenocrysts or microliths in various silica-undersaturated mafic-to-intermediate igneous rocks (alkali basalt, basanite, gabbro/syenite, nepheline syenite, olivine nephelinite, nepheline basanite, olivine-melilite nephelinite, phonolite and thephrite). It commonly coexists with Mg-Fe olivine, clinopyroxene, plagioclase, titanium magnetite, spinel ± Ti-Al augite ('fassaite'), kaersutite, melilite, K-Ba-feldspars, apatite, nepheline and leucite (Boivin, 1980; Kunzmann, 1989, 1999; Bonaccorsi *et al.*, 1990; Grapes *et al.*, 2003; Grew *et al.*, 2008). Daughter rhönite crystals from silicate melt inclusions in olivine phenocrysts were reported from alkali basalts of different volcanic fields (Sharigin *et al.*, 2011).

To date, kuratite has been found in only a few rock samples of terrestrial and extraterrestrial origin from ten natural occurrences: (1) melaphonolites of Puy de Saint-Sandoux (Grünhagen and Seck, 1972); (2) Ca-contaminated alkali basalt at the contact with corals, in Réunion Island (Havette *et al.*, 1982); (3) basanite in Scania, southern Sweden (Olsson, 1983); (4) kaersutite-bearing spinel-wehrlite xenoliths in Foster Crater, Antarctica (Gamble and Kyle, 1987); (5) tephrite and nepheline basanite in the Kaiserstuhl volcanic complex, SW Germany (Grapes and Keller, 2010);

(6) buchite (combustion metamorphic melt rock) in naturally burned coal beds, Želénky, Most Basin, North-Bohemian, Czech Republic (Žáček *et al.*, 2015); (7) D'Orbigny angrite meteorite (Mittlefehldt *et al.*, 2002; Kurat *et al.*, 2004; Hwang *et al.*, 2014, 2016); (8) plutonic igneous angrite NWA 4590 (Kuehner and Irving, 2007); (9) melt inclusions in augite grains of the Luna 24 regolith (Treiman, 2008); and (10) volcanic angrite SAHARA 99555 (Mittlefehldt *et al.*, 2002; Jambon and Boudouma, 2011).

We identified minerals of the rhönite–kuratite series in Ca-rich melilite- and nepheline-bearing paralavas from a recently discovered combustion metamorphic complex in the Choir–Nyalga basin, Central Mongolia (Fig. 1). The minerals contain variable amounts of Si, Ti, Mg, Fe²⁺ and Fe³⁺, and many compositions are close to kuratite. The paralava samples also contain microliths of low-Ti kuratite and Ti-poor minerals which approaches the unnamed Ti-free Fe²⁺-analogue of rhönite Ca₂Fe²⁺₄Fe³⁺₄[Si₄Al₂O₂₀] in the classification scheme of Kunzmann (1999). According to CNMNC recommendations for the sapphirine group (Grew *et al.*, 2008), the formula of this phase is Ca₄Fe²⁺₈Fe³⁺₄O₄[Si₈Al₄O₃₆]. The objectives of this study are to characterize mineral assemblages, phase compositions, and petrogenetic features of the Nyalga paralavas, as well as the composition of the minerals, which are extremely diverse and include very rare species of the rhönite–kuratite series. The formation conditions of rhönite and kuratite from terrestrial and extraterrestrial occurrences are compared with those for Fe³⁺-dominant varieties of rhönite subgroup (dorrite and khesinite).

Analytical methods

The bulk composition of paralava samples was analysed by X-ray fluorescence analysis (XRF) on a CPM-25 spectrometer using glass fusion discs, at the Institute of Geochemistry, Siberian Branch of the Russian Academy of Sciences (Irkutsk). Minerals, phases and silicate glasses in rock samples were investigated by scanning electron microscopy and energy-dispersive spectrometry (SEM-EDS) using a Carl Zeiss LEO-1430VP electron microscope equipped with an Oxford Instruments INCA Energy 350 analytical system, at the Geological Institute, Siberian Branch of the Russian Academy of Sciences in Ulan-Ude (analyst: E.A. Khromova). The quality of analyses

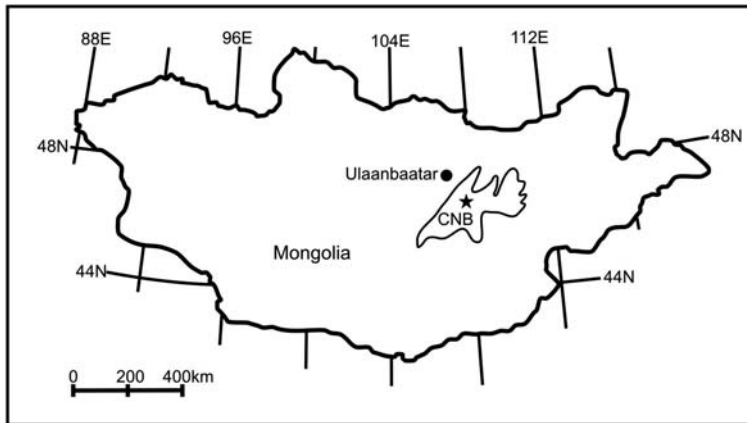


FIG. 1. Location map of the Choir–Nyalga basin (CNB) and the Tugrug brown coal quarry (star, coordinates $46^{\circ}53'07''\text{N}$, $108^{\circ}02'55''\text{E}$) in Central Mongolia, modified after Erdenetsogt *et al.* (2009).

was checked with reference to samples of quartz, albite, orthoclase, wollastonite, MgO , Al_2O_3 , CaF_2 , NaCl and metals recommended as Reference Standards for X-Ray Microanalysis (reg. num. 6316) by Micro-Analysis Consultants Limited (Oxford Instruments Ltd.). Matrix effects were taken into account using the *XPP* algorithm of the proprietary software of the INCA Energy 350 analytical system. The analyses were carried out at an accelerating voltage of 20 kV, a beam current of 0.5 nA and a counting time of 50 s. For these analytical conditions, the metrological characteristics were determined for analysis of minerals and silicate glasses. The detection limit for SEM-EDS was 0.2–0.3 wt.%, and the average random errors were 0.9%, 3% and 13% for elements existing in the concentrations >10 wt.%, 1–10 wt.% and 0.3–1 wt.%, respectively (Lavrent'ev *et al.*, 2015). Silicate glasses and minerals were analysed by scanning over $>10 \mu\text{m}^2$ rectangular spots (for phases exceeding this size). These analytical conditions reduced considerably the losses of alkalis from glasses.

The Raman spectra were measured on a Horiba Jobin Yvon LabRam HR800 confocal micro-Raman spectrometer, equipped with an Olympus BX-41 optical polarization microscope, at the Sobolev Institute of Geology and Mineralogy in Novosibirsk. In order to obtain good spectra from small (down to $2 \mu\text{m}$) phases, a $100\times$ objective was used and the pinhole sizes were set to 50–100 μm . The samples were excited by the 532 nm wavelength of a 50 mW Nd:YAG laser. The spectra were recorded by a liquid-nitrogen cooled Horiba Scientific Symphony II CCD detector.

Combustion metamorphic melt rocks: geological background

While sampling a trachybasalt-trachyte-trachyrhyolite volcanic complex in the Choir–Nyalga basin, Central Mongolia (Fig. 1), during the field trip of 2014, we (I.S. Peretyazhko and E.A. Savina) discovered three conical and elongate sedimentary outliers, 150–450 m wide at the base and 25–35 m high, with melt rocks looking like volcanic lava or scoria on their tops. The outcrops and disintegrated pieces of melt rocks were restricted to the tops of the outliers (we called them Crown, Camel and Baby), which are remnants of eroded layered sediments mostly buried under recent Quaternary sediments and vegetation (Fig. 2).

The Choir–Nyalga basin sediments composed of mudstone, siltstone, carbonate-silicate and carbonate rocks with brown coal intercalations were deposited in the Early Cretaceous (Erdenetsogt *et al.*, 2009) after trachybasaltic, trachytic and trachyrhyolitic eruptions associated with intraplate continental rifting that acted over a large territory of Central Mongolia. Trachyrhyolites from the Nyalga basin were studied previously by Peretyazhko *et al.* (2014). Melt rocks similar to volcanic lavas and slags were also found 4–5 km far from the three outliers, near the Tugrug brown coal quarry (Fig. 1), in bulldozer ditches stripping the sedimentary sequence.

The Nyalga melt rocks formed no later than 2 Ma ago (our unpublished K/Ar data) by melting of mudstone, siltstone and iron-bearing carbonate-silicate sediments during combustion of brown



FIG. 2. Outliers Crown (a) and Camel (b): remnants of eroded layered sediments mostly buried under recent Quaternary sediments and vegetated.

coal. The carbonate-silicate rocks were, specifically, calcite-dolomite limestones with detrital quartz and feldspar; mudstones with siderite-bearing layers and lenses; and sandstone with Ca-Mg-Fe carbonate and carbonate-sulfate cement. By analogy with volcanics, the Nyalga melt rocks correspond to Al-rich dacites (61–68 wt.% SiO₂) and Ca-bearing silica-undersaturated mafic rocks (38–44 wt.% SiO₂) with melilite, clinopyroxene, plagioclase and nepheline (olivine-melilite nephelinites). According to the terminology for combustion metamorphic or pyrometamorphic melt rocks (Foit *et al.*, 1987; Cosca *et al.*, 1989), they are, respectively, clinkers and paralavas. See Table 1 for XRF analyses of bulk composition of several paralava samples and SEM EDS analyses of matrix glasses.

Clinkers, the predominant variety of melt rocks in the Nyalga complex, look like felsic volcanics or obsidian. They are purple, pink, reddish-brown, or variegated in colour, glassy and massive, sometimes vesicular, with an Si-Al-rich glass matrix. The glass encloses partially molten quartz and plagioclase (andesine) grains, as well as rare inclusions of titanium magnetite, rutile and zircon. The mineral inclusions survived after partial melting of sediments, presumably mudstones and/or siltstones.

Other phases found in the glass are frequent 50–100 µm euhedral grains with hexagonal cross sections and tabular prismatic crystals of minerals with their compositions intermediate between indialite and its Fe²⁺-dominant analogue ferroindialite. Their presence indicates melting of mudstones and/or siltstones at temperatures exceeding 1000–1100°C (Schreyer *et al.*, 1990; Balassone *et al.*, 2004).

Clinkers in many outcrops and samples are crosscut by thin veins of dark-to-black massive paralava which enclose numerous xenoliths of vesicular clinker curved by melt flow, with partially fused margins. Paralavas most commonly abound in vesicles (former gas voids) and contain clinker and sedimentary xenoliths. There are some metre-sized blocks of massive fine-grained and well-crystallized paralavas and numerous irregularly shaped ‘stones’ formed by quenching of flowing paralava melts.

Results

The matrix of paralavas is composed of 200–400 µm melilite and clinopyroxene ± plagioclase and Mg-Fe olivine microphenocrysts, with nepheline and residual glasses in interstices between them. The interstitial phases contain numerous microliths

MINERALS OF THE RHÖNITE-KURATITE SERIES IN PARALAVAS

TABLE 1. Bulk rock (XRF) and glass (SEM EDS) compositions and CIPW norms^a of paralavas from the Nyalga combustion metamorphic complex.

Sample	MN-1127			MN-1287			MN-1128			MN-1129			MN-1133		MN-1171		MN-1174		MN-1192			
	Rock	GI (36)	GI (4)	Rock	GI (12)	GI (5)	GI (13)	GI (12)	GI (7)	GI (4)	GI (8)	GI (35)	Rock	Rock	Rock	Rock	Rock	Rock	Rock	Rock		
Analysis	1	2	3	4	5	6	7	8	9	10	11	12	13	10	11	12	13	10	11	12	13	
SiO ₂	38.18	39.01	52.06	39.97	43.20	43.51	53.07	39.39	67.33	38.89	37.65	40.73	42.95	38.89	37.65	40.73	42.95	38.89	37.65	40.73	42.95	
TiO ₂	1.03	0.22		0.98	0.24	0.11		0.00	1.17	1.04	1.15	0.97	0.94	1.04	1.15	0.97	0.94	1.04	1.15	0.97	0.94	
Al ₂ O ₃	15.97	20.95	38.70	16.80	22.26	21.92	31.47	22.08	16.93	15.45	16.56	16.83	15.42	15.45	16.56	16.83	15.42	15.45	16.56	16.83	15.42	
Fe ₂ O ₃	1.85			2.60						1.37	0.74		0.45	1.37	0.74		0.45	1.37	0.74		0.45	
FeO	10.06	4.73 ^b	0.55 ^b	10.96	4.42 ^b	4.77 ^b	0.23 ^b	4.69 ^b	3.38 ^b	8.62	5.93	5.75	8.98	8.62	5.93	5.75	8.98	8.62	5.93	5.75	8.98	
MnO	0.21			0.19						0.22	0.19	0.19	0.32	0.22	0.19	0.19	0.32	0.22	0.19	0.19	0.32	
MgO	7.03			6.36						7.83	8.45	8.36	7.19	7.83	8.45	8.36	7.19	7.83	8.45	8.36	7.19	
CaO	22.55	4.44		17.69	2.29	5.42		3.06	0.44	22.55	24.42	20.89	19.72	22.55	24.42	20.89	19.72	22.55	24.42	20.89	19.72	
Na ₂ O	1.52	3.94	1.54	0.69	5.22	3.09	2.45	5.03	2.47	1.56	0.77	1.02	0.70	1.56	0.77	1.02	0.70	1.56	0.77	1.02	0.70	
K ₂ O	0.48	12.71	4.90	0.59	12.92	10.49	10.32	12.43	5.11	0.61	0.33	0.59	0.91	0.61	0.33	0.59	0.91	0.61	0.33	0.59	0.91	
P ₂ O ₅	0.08			0.08						0.06	0.05	0.07	0.07	0.06	0.05	0.07	0.07	0.06	0.05	0.07	0.07	
LOI	0.83			2.41						1.38	3.34	4.94	1.26	1.38	3.34	4.94	1.26	1.38	3.34	4.94	1.26	
Total	99.79	86.00	97.74	99.32	90.55	89.31	97.54	86.68	98.35	99.58	99.57	101.13	98.91	99.58	99.57	101.13	98.91	99.58	99.57	101.13	98.91	
X _{Mg}	0.53			0.48						0.60	0.71	0.71	0.58	0.60	0.71	0.71	0.58	0.60	0.71	0.71	0.58	
Q			23.89						27.57													
C			30.86				16.27		4.59													
Or			28.96				60.99		30.20													
Ab			13.03				19.04		20.90													
An	35.76	2.26		42.43		16.72		1.11	7.49	34.03	42.39	41.21	37.17	34.03	42.39	41.21	37.17	34.03	42.39	41.21	37.17	
Hy			1.01						5.37													
Lc	2.27	43.32		2.83	55.37	54.45		41.36		2.87	1.58	2.83	4.31	2.87	1.58	2.83	4.31	2.87	1.58	2.83	4.31	
Ne	7.06	20.99		3.25	25.45	15.86	0.92	26.59		7.29	3.67	4.86	3.25	7.29	3.67	4.86	3.25	7.29	3.67	4.86	3.25	
Kp		18.24			7.79			18.18														
Ns					0.41																	
Di	2.64			17.75		4.85				7.04	1.41	18.08	31.12	7.04	1.41	18.08	31.12	7.04	1.41	18.08	31.12	
Ol	27.26	7.47		23.37	6.58	5.43	0.33	7.67		24.6	23.33	17.37	14.45	24.6	23.33	17.37	14.45	24.6	23.33	17.37	14.45	
Cs	22.84	7.23		8.25	3.89	2.46		5.08		22.02	25.24	13.58	7.71	22.02	25.24	13.58	7.71	22.02	25.24	13.58	7.71	
Ilm	1.98	0.49		1.94	0.51	0.23			2.22	2.01	2.26	1.92	1.84	2.01	2.26	1.92	1.84	2.01	2.26	1.92	1.84	
Ap	0.19			0.19						0.14	0.12	0.16	0.16	0.14	0.12	0.16	0.16	0.14	0.12	0.16	0.16	
Ne/(Ne+Lc)	0.76	0.33		0.53	0.31	0.23		0.39		0.72	0.70	0.63	0.43	0.72	0.70	0.63	0.43	0.72	0.70	0.63	0.43	

^aCalculated with all iron as FeO.

^bAll Fe as FeO. GI (n) = Glass (numerals in parentheses are numbers of analyses). X_{Mg} = MgO/(MgO+FeO+Fe₂O₃), mol.%. LOI is loss on ignition recalculated to account for FeO and Fe₂O₃ proportions. Blanks in glass analysis indicate values below SEM EDS detection limits. Location of samples: Crown outlier (MN-1127, MN-1128, MN-1129 and MN-1287); Camel outlier (MN-1133, MN-1171 and MN-1174); vicinity of Camel outlier (MN-1192). CIPW norms: Q = quartz, C = corundum, Or = orthoclase, Ab = albite, An = anorthite, Hy = hypersthene, Lc = leucite, Ne = nepheline, Kp = kaliophillite, Ns = Na metasilicate, Di = diopside, Ol = olivine, Cs = Ca orthosilicate, Ilm = ilmenite, Ap = apatite.

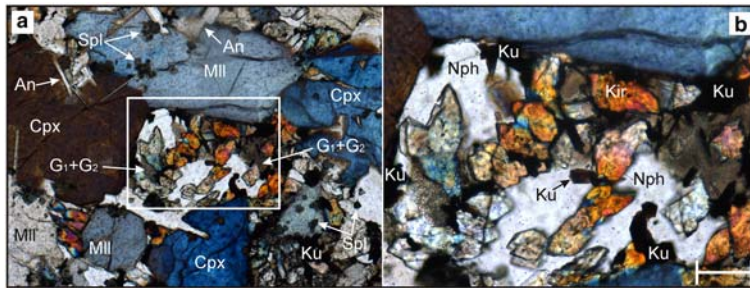


FIG. 3. Paralava fragment from sample MN-1127 (a) and kuratite crystals in interstices between microphenocrysts (b). White box in panel (a) frames the fragment enlarged in panel (b). Mineral names are abbreviated as Mll = melilite, Cpx = Al-clinopyroxene, An = anorthite, Spl = spinel (Fe-rich spinel), G_1+G_2 = Si-Al-K and Si-Al-Ca-Fe glasses (microemulsion of quenched melts), Nph = nepheline, Kir = kirschsteinite (with inclusions of Ca-bearing fayalite), and Ku = kuratite. Polarized light. Scale bar in (b) is 50 μm .

and crystals of Fe-Ca olivines, pyrrhotite and other phases, including minerals of the rhönite–kuratite series (Fig. 3; Table 2). The compositions of melilite, clinopyroxene, olivine, plagioclase, K-Ba feldspars and spinel-group minerals from paralavas are plotted in diagrams of Figs 4–8; the compositions of accessory minerals are given in Table 3.

Compositions of main phases in paralavas

Melilite varies in molar percentages of end-members in different samples (Fig. 4): 10–85 mol.% åkermanite ($\text{Ca}_2\text{MgSi}_2\text{O}_7$), 0–42 mol.% ferroåkermanite ($\text{Ca}_2\text{Fe}^{2+}\text{Si}_2\text{O}_7$) and 15–75 mol.% gehlenite ($\text{Ca}_2\text{Al}_2\text{SiO}_7$) + ferrigehlenite ($\text{Ca}_2\text{Fe}^{3+}\text{AlSiO}_7$). The percentages of ferroåkermanite and gehlenite + ferrigehlenite end-members are approximately equal in most melilites but the contents of åkermanite vary in a broad range (Fig. 4). Åkermanite and gehlenite in melilites are especially variable in the paralavas that contain partially molten clinker xenoliths (samples MN-1128 and MN-1129) and inclusions of xenogenic mineral aggregates (samples MN-1176 and MN-1193). Melilite microphenocrysts are quite homogeneous compositionally but have more ferrous rims. The contents of alkalis are <3.7 wt.% Na_2O and <0.6 wt.% K_2O .

Most clinopyroxenes are Al-rich diopside–hedenbergites (Fig. 5). Al-clinopyroxene microphenocrysts are typically magnesian species with $\text{Mg}\# = \text{Mg}/(\text{Mg} + \text{Fe}^{2+} + \text{Fe}^{3+})$ from 0.6 to 0.8, up to 16 wt.% Al_2O_3 and 1–2 wt.% TiO_2 . The rims are higher in FeO, SiO_2 and MnO (up to 0.8 wt.%) than the cores but more depleted in Al_2O_3 , MgO ($\text{Mg}\# =$

0.24–0.42), TiO_2 (0.6–0.8 wt.%) and approach hedenbergites (Fig. 5).

Many (but not all) samples contain elongate euhedral anorthite and anorthite–bytownite crystals (Fig. 6a). Plagioclases contain up to 2 wt.% FeO and <0.5 wt.% K_2O . Most of the plagioclase microphenocrysts are polysynthetically twinned. K-Ba-feldspars found in some samples vary from celsian (>30 mol.% Ba) to hyalophane and Ba-orthoclase (<30 mol.% Ba) with 1.5–5 wt.% SrO (Fig. 6b; Table 3, an. 1, 2, 7).

Similarly, olivine compositions vary from sample to sample (Fig. 7). All paralava samples contain microliths of both Ca-bearing fayalite with inclusions of kirschsteinite and kirschsteinite with inclusions of Ca-bearing fayalite in different relative amounts (Figs 12a–d, 13a,b,e and 14a,d). The contents of fayalite (Fe_2SiO_4) and larnite (Ca_2SiO_4) end-members are 70–85 and 7–15 mol.% in Ca-bearing fayalite and 40–60 and 35–45 mol.% in kirschsteinite, respectively. Microphenocrysts of Mg-Fe olivine, an intermediate member of the fayalite–forsterite series (hortonolite), were found in a sample MN-1287. They have rims with lower contents of forsterite (45 mol.% against 75 mol.% in the core) and higher CaO and MnO (3.2 and 0.9 wt.%, respectively). Monticellite and Ca-bearing forsterite are found in segregations of xenogenic mineral aggregates (remnant xenoliths of carbonate-silicate sedimentary rocks) from many samples (MN-1133, MN-1193 and others).

Octahedral or cubic-octahedral euhedral spinel-group minerals are commonly enclosed in Al-clinopyroxene and melilite microphenocrysts or occur in interstices between matrix minerals (Figs 3, 12a,c, 13d,e and 14b,c). Most of them

TABLE 2. Compositions (SEM EDS) and crystal chemical formulas for minerals of the rhönite–kuratite series in paralavas from the Nyalga combustion metamorphic complex.

Analysis	MN-1127		MN-1128		MN-1129		MN-1133			MN-1175			MN-1176		MN-1193	
	1	2	3(4)	3(3) ^c	1(1) ^c	5	6	7	8	9	10	11	12	13	14	15
SiO ₂	24.74	23.91	24.55	26.43	26.29	26.83	26.49	26.79	27.32	27.87	25.34	26.35	27.53	28.62	25.27	24.94
TiO ₂	7.49	8.80	6.51	1.33	0.58	2.92	9.83	7.00	4.43	0.26	6.87	1.88	10.91	3.27	2.25	5.79
Al ₂ O ₃	15.63	15.45	15.29	14.76	15.12	14.44	14.97	15.23	17.61	17.08	16.77	15.05	16.31	19.06	16.21	14.87
FeO ^d	36.62	35.12	37.97	42.51	40.02	40.71	26.14	34.75	33.53	43.03	33.06	41.57	20.08	29.58	38.76	38.66
MnO	0.26	0.48	0.19	0.19	0.80	0.32	0.47	0.56	0.53	0.59	0.51	0.89	0.63	0.79	0.98	
MgO	2.58	3.20	2.57	1.31	1.41	0.70	8.13	3.05	3.85	4.36	4.36	1.56	12.40	6.40	2.19	2.07
CaO	12.33	12.33	12.17	10.99	11.85	11.67	11.44	11.68	12.23	11.83	12.37	12.07	13.29	13.22	12.76	13.61
Na ₂ O	0.34	0.17	0.26	0.47	0.57	0.64	0.35	0.27	0.37	0.52	0.15	0.35				
Total	99.98	99.45	99.30	97.99	96.64	98.23	97.81	99.33	99.88	101.18	99.42	99.72	100.52	100.78	98.23	100.92
Formula contents per 28 cations and 40 oxygens																
Ca	3.799	3.820	3.780	3.463	3.758	3.679	3.472	3.608	3.690	3.607	3.771	3.735	3.802	3.869	3.984	4.181
Na	0.187	0.098	0.143	0.270	0.327	0.365	0.193	0.153	0.203	0.287	0.083	0.196				
Si	7.117	6.915	7.118	7.776	7.782	7.895	7.504	7.724	7.691	7.933	7.211	7.609	7.350	7.817	7.364	7.151
^v Al	4.883	5.085	4.882	4.224	4.218	4.105	4.496	4.276	4.309	4.067	4.789	4.391	4.650	4.183	4.636	4.849
^{vi} Al	0.415	0.180	0.343	0.895	1.057	0.903	0.504	0.900	1.534	1.663	0.835	0.732	0.482	1.952	0.931	0.176
Fe ²⁺	7.396	7.318	7.359	7.447	6.676	7.745	6.192	7.883	6.792	7.665	6.772	7.002	4.483	5.868	6.727	7.096
Fe ³⁺	1.414	1.176	1.846	3.012	3.231	2.274	0.000	0.495	1.101	2.580	1.097	3.038	0.000	0.888	2.719	2.175
Ti	1.620	1.914	1.418	0.294	0.129	0.646	2.004	1.517	0.938	0.056	1.470	0.408	2.190	0.672	0.493	1.249
Mg	1.104	1.378	1.110	0.573	0.622	0.307	3.432	1.310	1.615	1.851	0.670	4.935	2.606	0.951	0.885	
Mn	0.064	0.116	0.047	0.201	0.080	0.112	0.136	0.14	0.126	0.142	0.123	0.218	0.146	0.195	0.238	
X _{Mg}	0.13	0.16	0.13	0.07	0.09	0.04	0.36	0.14	0.19	0.00	0.21	0.09	0.52	0.31	0.12	0.11

^aQuantity of crystals.

^bQuantity of analyses.

^cCompositions of Ti-poor minerals which approaches the Ti-free Fe²⁺-analogue of rhönite Ca₄Fe₈²⁺Fe₄³⁺O₄[Si₈Al₄O₃₆].

^dAll Fe is expressed as FeO.

X_{Mg} = Mg/(Mg+Fe²⁺). Fe²⁺ and Fe³⁺ from mineral stoichiometry.

Blanks indicate values below SEM EDS detection limits.

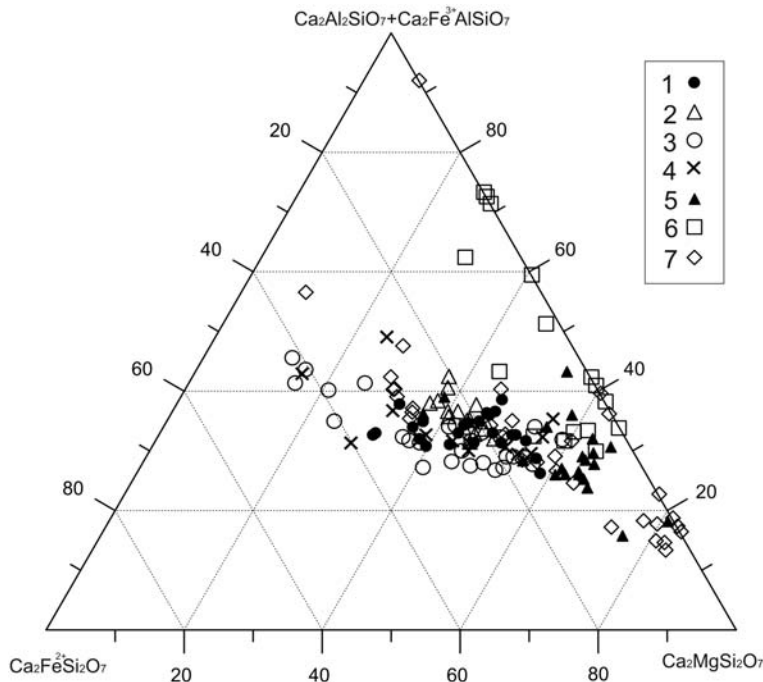


FIG. 4. Classification of melilites from paralavas according to contents of åkermanite ($\text{Ca}_2\text{MgSi}_2\text{O}_7$), ferroåkermanite ($\text{Ca}_2\text{Fe}^{2+}\text{Si}_2\text{O}_7$), gehlenite ($\text{Ca}_2\text{Al}_2\text{SiO}_7$) and ferrigehlenite ($\text{Ca}_2\text{Fe}^{3+}\text{AlSiO}_7$) end-members. Symbols refer to samples MN-1127 (1), MN-1287 (2), MN-1128 (3), MN-1129 (4), MN-1133 (5), MN-1176 (6) and MN-1193 (7).

belong to the spinel (MgAl_2O_4) – hercynite (FeAl_2O_4) join with Fe^{3+} impurity (Fig. 8) and minor TiO_2 (within 2.4 wt.%); Fe^{3+} contents are relatively high in hercynite (Fig. 8). A few paralava samples (MN-1127, MN-1129 and some others) contain magnetite and Al-magnetite with minor magnesioferrite (Fig. 8) and titanium magnetite (Fig. 13a) with its composition intermediate between magnetite and ulvöspinel (Table 3, an. 4, 5).

Compositions and Raman spectroscopy of rhönite–kuratite series minerals

Minerals of the rhönite–kuratite series were found in twelve paralava samples from the Nyalga combustion metamorphic complex. Analyses were performed using SEM-EDS on 71 crystals and microliths of the minerals in eight paralava samples. Average element contents and crystal chemical formulas of phases based on 28 cations and 40 oxygens are listed in Table 2. Most of the minerals are kuratites (Hwang *et al.*, 2014, 2016) or an Fe^{2+} -dominant analogue of rhönites (Grew *et al.*, 2008; Grapes and Keller, 2010) identified on the

basis of Fe^{2+} content, $X_{\text{Mg}} = \text{Mg}/(\text{Mg} + \text{Fe}^{2+})$ between 0.36 and 0–0.04 (Table 2), and Mg/Fe^{2+} ratio (Fig. 9). The compositions of the Nyalga rhönite–kuratite series minerals plotted on the $(\text{IV})\text{Si}_i^{(\text{VIII})}(\text{Na} + \text{K})$ vs. $(\text{VI})\text{Ti}^{4+}$ classification diagram of the sapphirine supergroup (Fig. 10) are mostly lower in Ti (<2 apfu) than kuratites from other occurrences. The compositions are of two groups with Ti contents 2.4–1.2 and 1.0–0.0 apfu and change regularly from the kuratite $\text{Ca}_4\text{Fe}_{10}^{2+}\text{Ti}_2\text{O}_4[\text{Si}_8\text{Al}_4\text{O}_{36}]$ and rhönite $\text{Ca}_4(\text{Mg}, \text{Fe}^{2+})_8\text{Fe}_8^{3+}\text{Ti}_2\text{O}_4[\text{Si}_6\text{Al}_6\text{O}_{36}]$ to low-Ti kuratite (1.6–1.0 apfu Ti) and Ti-poor minerals (<1.0 apfu Ti) which approaches the unnamed Ti-free Fe^{2+} -analogue of rhönite $\text{Ca}_4\text{Fe}_8^{2+}\text{Fe}_4^{3+}\text{O}_4[\text{Si}_8\text{Al}_4\text{O}_{36}]$ (Fig. 10).

We measured the Raman spectra of rhönite–kuratite series minerals in paralava samples MN-1133, MN-1127 and MN-1129 (Fig. 11a). Kuratites in MN-1133 and MN-1127 have mostly variable relative contents of Fe^{2+} and Mg ($X_{\text{Mg}} = 0.13$ –0.19) with 1.6–0.9 apfu Ti (Table 2, Fig. 10). These kuratites show spectra with five scattering peaks near 133–155 cm^{-1} (strong), 399–401, 545–566,

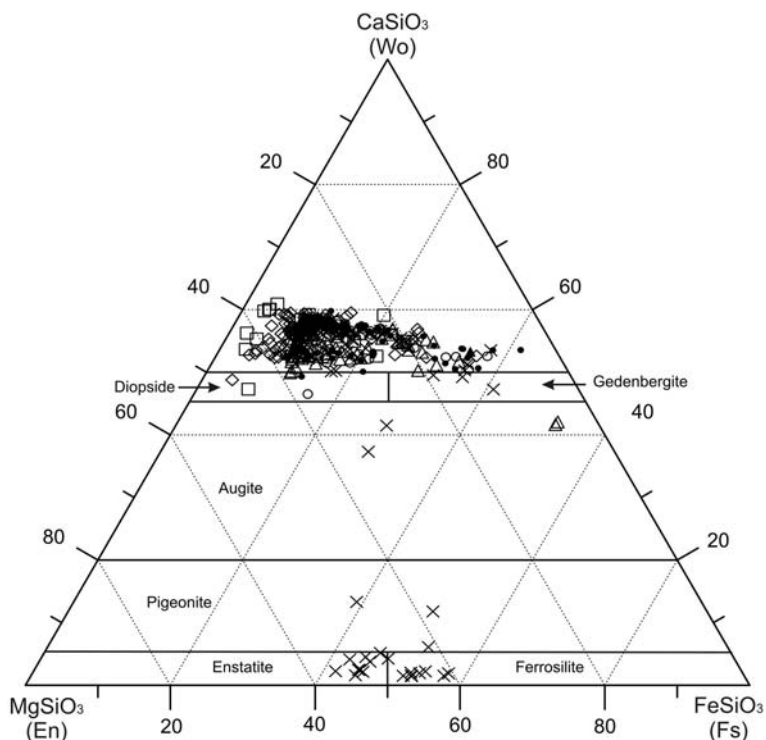


FIG. 5. Classification of clinopyroxenes from paralavas according to contents of wollastonite (Wo), enstatite (En) and ferrosilite (Fs) end-members. Symbols are the same as in Fig. 4.

684–693 cm^{-1} (strongest) and at 828–839 cm^{-1} . Their spectra are similar in shape to that of IMA 2013-109 kuratite (Fig. 11b) but have peaks shifted to lower frequencies, probably due to a different composition. The peak about 980–996 cm^{-1} reported for the IMA 2013-109 kuratites and the Luna 24 regolith is small or absent in the MN-1133 and MN-1127 paralavas. Furthermore, the Nyalga and IMA 2013-109 kuratites lack the weak shoulder at 720 cm^{-1} at the strongest scattering peak of 670 cm^{-1} found in the Luna 24 kuratite spectra (Treiman, 2008). The Raman spectra of the Ti-poor Fe^{2+} -analogue of rhönite ($X_{\text{Mg}} = 0.04\text{--}0.09$) in sample MN-1129 also have shapes as in the spectra of kuratites from other paralava samples, but the peaks are notably smaller at the same operation conditions (Fig. 11a). Compared to the spectrum of kuratite, RRUF rhönite (060316, <http://rruff.info>) has a stronger peak at 525 cm^{-1} in the 500–600 cm^{-1} range, which is shifted to lower frequencies, but a smaller peak at 715 cm^{-1} (650–750 cm^{-1} range) shifted to higher frequencies.

Mineral assemblages of paralava samples containing minerals of the rhönite–kuratite series

Sample MN-1127 from the Crown outlier (Fig. 2a) is a massive paralava (Table 1, an. 1) containing melilite and Al-clinopyroxene microphenocrysts with Fe-rich rims and anorthite ($\text{An}_{99\text{--}93}$) microliths (Figs 4–6a). Many melilite and Al-clinopyroxene microphenocrysts and interstices between matrix minerals host microliths of an intermediate variety of the spinel-hercynite series (Figs 3, 8 and 13b). The paralava matrix encloses sporadic mottles of brown glass (up to ~ 1 cm across) with high Al_2O_3 reaching 39 wt.% (Table 1, an. 3), which are surrounded by aggregates of anorthite–bytownite and Al-clinopyroxene microliths.

Interstices between microphenocrysts are filled with nepheline and Si-Al-K glass (Fig. 3; Table 1, an. 2). Microlith-free zones in Si-Al-K glass rarely exceed 20–30 μm . Many zones of Si-Al-K glass include abundant globules (droplets) of sub-micrometre and μm -sized glass (Figs 3 and 13b)

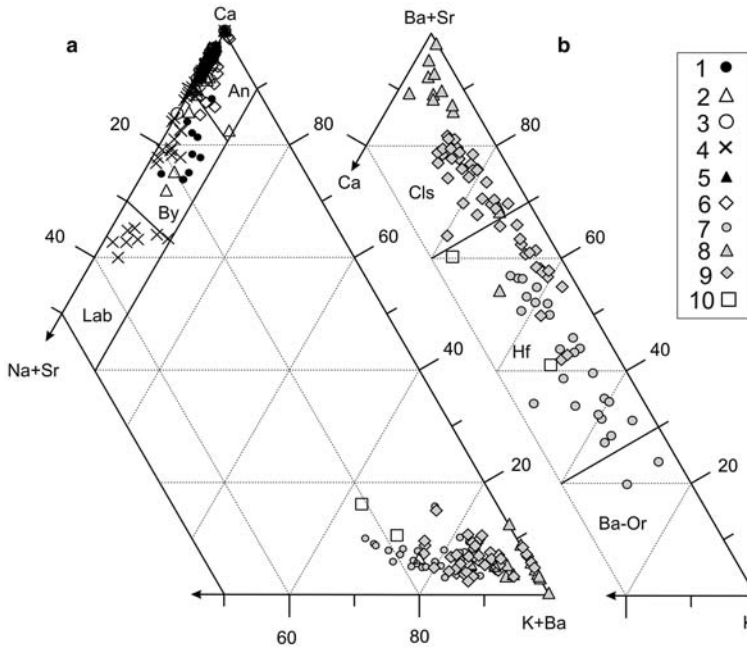


FIG. 6. Ca – (K+Ba) – (Na+Sr) and (Ba+Sr) – K – Ca diagrams of plagioclase and K-Ba feldspar (X -site, apfu) from paralavas. The diagrams show continuous feldspar variations as anorthite (An), bytownite (By) and labradorite (Lab) (left diagram, *a*) and as celsian (Cls), hyalophane (Hf) and K-Ba orthoclase (Ba-Or) (right panel, *b*). Plagioclases are from samples MN-1127 (1), MN-1287 (2), MN-1128 (3), MN-1129 (4), MN-1133 (5), MN-1176 (6); K-Ba feldspars are from samples MN-1127 (7), MN-1133 (8), MN-1193 (9) and MN-1176 (10).

with Si, Al, Ca and Fe enrichment and, possibly, with high H₂O contents inferred from a 10–15 wt.% deficit of totals. The Si-Al-K glass encloses numerous needle-like crystals (Fig. 12*a,b*) with their Raman spectra corresponding to goethite and compositions with impurity of TiO₂ (3–8 wt.%), Al₂O₃ (3–12 wt.%) and MgO (1–3 wt.%). There are also quite numerous acicular and hopper crystals of glass-bearing goethite (Fig. 13*b*). Goethite may replace Al-magnetite or could form at devitrification of hydrous Fe-bearing residual glass (see below).

Nepheline and Si-Al-K glass enclose microliths of Ca-bearing fayalite and kirschsteinite, crystals of hyalophane, kuratite, and pyrrhotite globules (Figs 3, 12*a,b* and 13*a,b*). Hyalophane grows over anorthite and Al-clinopyroxene microphenocrysts but more often forms elongate euhedral crystals up to 100 μ m long. It has large ranges of Ba and K (Fig. 6*b*; Table 3, an. 1, 2) and 11–15 wt.% K₂O in rims, which correspond to Ba-orthoclase. Some 50–70 μ m vesicles in the paralava matrix are filled with calcite and Sr-rich baryte (Table 3, an. 3).

Kuratite occurs as euhedral crystals and intergrowths, up to 150–200 μ m long and up to 20–30 μ m across (Figs 3 and 12*a,b*), and shows minor compositional variations ($X_{\text{Mg}} = 0.10\text{--}0.15$; Table 2, an. 1). It crystallized together with the microliths of hyalophane and kirschsteinite containing inclusions of Ca-bearing fayalite. Kuratite crystals are greyish-brown (Fig. 3) and almost opaque in thin sections, with greenish brown to dark reddish brown pleochroism.

Sample MN-1287 from the Crown outlier (Fig. 2*a*) is a massive fine-grained paralava (Table 2, an. 4) with a matrix consisting of melilite, Al-clinopyroxene, anorthite (An_{100–93}), hortonolite microphenocrysts, and Fe-rich spinel – Mg-rich hercynite microliths (Figs 4–6*a*, 7 and 8). Zoned spinel crystals (Fig. 13*d*) grow over rims of Fe³⁺-bearing hercynite and show an increase of FeO (11 to 42 wt.%) and a decrease of Al₂O₃ (63 to 45 wt.%) and MgO (20 to 3 wt.%) from core to rim.

Nepheline coexists with a ferrous-silicate aggregate (palagonite), which has variable contents of Si, Al, Ca, Fe and, possibly, a high H₂O

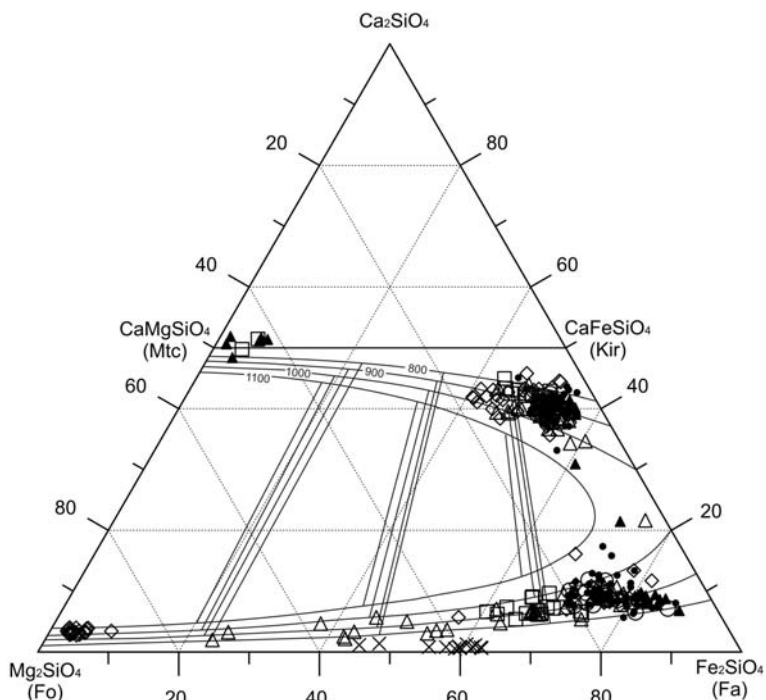


FIG. 7. Classification of olivines from paralavas according to the contents of forsterite (Fs) Mg_2SiO_4 , fayalite (Fa) Fe_2SiO_4 , monticellite (Mtc) CaMgSiO_4 and kirschsteinite (Kir) CaFeSiO_4 end-members. Isotherms of miscibility gap and solid tie lines are after Davidson and Mukhopadhyay (1984). Symbols are the same as in Fig. 4.

concentration indicated by a 20–25 wt.% deficit of totals. Palagonite replaces residual Si-Al-Ca-Fe glasses and encloses pyrrhotite globules, microliths of Fe-Ca olivines (Fig. 7), kuratite ($X_{\text{Mg}} = 0.14\text{--}0.20$), Ba-orthoclase and needles of baryte and Sr-rich baryte. Other interstitial phases are Si-Al-K glass (Table 1, an. 5), kuratite microliths and goethite needles. Some kuratites ($X_{\text{Mg}} = 0.12\text{--}0.22$) in Si-Al-K glass enclose titanium magnetite inclusions.

The sample contains 1–2 cm pyrrhotite segregations with drop-shaped inclusions of wüstite partially replaced by magnetite (Fig. 13c) compositionally similar to the $\text{Fe}^{2+}\text{Fe}_2^{3+}\text{O}_4$ end-member, as well as a zoned segregation with a pyrrhotite margin around an aggregate of acicular goethite, an oxygen-rich Ca-F phase similar to fluorite, and calcite (Fig. 12c). Pyrrhotite in these segregations encloses up to 50 μm long euhedral kuratite crystals ($X_{\text{Mg}} = 0.16$; Table 2, an. 2) intergrown with kirschsteinite. Some vesicles (former gas bubbles) have transparent gypsum crystals on their walls and some are filled with a calcite-siderite aggregate.

Samples MN-1128 and MN-1129 from the Crown outlier (Fig. 2a) are massive fine-grained paralavas with partially molten lilac clinker xenoliths, abundant especially in MN-1129. The matrix consists of melilite, Al-clinopyroxene with Fe-rich rims and anorthite-bytownite (An_{100-87}) microphenocrysts (Figs 4–6a). Plagioclase in sample MN-1129 varies from bytownite to labradorite (An_{90-60}) towards clinker xenoliths. The interstitial phases are nepheline and Si-Al-K glass (Table 1, an. 6, 8) with microliths of Ca-bearing fayalite and kirschsteinite in different relative amounts. The glass includes P-rich zones (up to 4 wt.% P_2O_5) in sample MN-1128 and contains impurities of Ba (1–1.5 wt.% BaO) and Sr (1.6–2.3 wt.% SrO) in MN-1129. The matrix in MN-1128 encloses sporadic mottles of Al-rich brown glass (300–500 μm across) (Table 1, an. 7).

Al-clinopyroxene and melilite microphenocrysts, as well as their interstices, host inclusions of Fe-rich spinel with hercynite rims enriched in Fe^{3+} ($\text{Fe}^{2+}/(\text{Mg}+\text{Fe}^{2+}) = 0.83\text{--}0.85$; Fig. 8). Near clinker xenoliths in sample MN-1129, there are

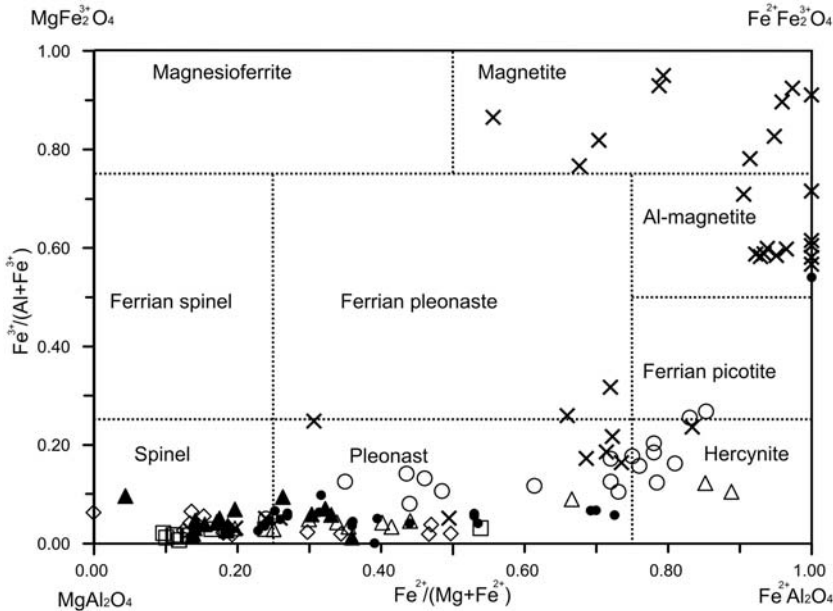


FIG. 8. Binary classification diagram showing Mg vs. Fe²⁺ and Al vs. Fe³⁺ cation exchange in spinel-group minerals from paralavas. Field contours are according to Haggerty (1991) and Deer *et al.* (1992). Symbols are the same as in Fig. 4.

segregations of magnetite and Al-magnetite with up to 40 mol.% magnesioferrite (Fig. 8), as well as pyroxene with compositions intermediate between ferrosilite and enstatite with very low Ca (Fig. 5).

Nepheline from sample MN-1128 encloses euhedral kuratite ($X_{Mg} = 0.12\text{--}0.15$; Table 2, an. 3) and the Ti-poor Fe²⁺-analogue of rhönite ($X_{Mg} = 0.06\text{--}0.08$; Table 2, an. 4), while Si-Al-K glass contains fine needles of goethite (Fig. 12*d*), siderite, calcite, pyrrhotite globules, and a palagonite aggregate. The Ti-poor Fe²⁺-analogue of rhönite crystallized in the micro-emulsion of immiscible melts and grew on Al-magnetite microliths (Fig. 12*d*). Interstitial Si-Al-K glass in sample MN-1129 hosts numerous submicrometre globules of Si-Al-Ca-Fe glass (microemulsion of quenched melts, Fig. 12*f*) and commonly also minerals of the rhönite–kuratite series with TiO₂ decreasing from 3.5–2 to 1.7–0.6 wt.% and K₂O increasing to 3.6 wt.% from core to rim ($X_{Mg} = 0.04\text{--}0.09$; Table 2, an. 5, 6). Euhedral microliths of the Ti-poor Fe²⁺-analogue of rhönite ($X_{Mg} = 0.09$) in Si-Al-K glass coexist with goethite and palagonite replacing Si-Al-Ca-Fe glass (Fig. 12*e*).

Euhedral grains with hexagonal cross sections and tabular crystals of K-bearing (0.8–1.7 wt.%

K₂O) indialite with average $X_{Mg} = 0.66$ (Table 3, an. 6) are commonly observed among dacitic glass (Table 1, an. 9) of lilac clinker xenoliths (see Raman spectra of indialite from sample MN-1129 in Fig. 15*a*). The excitation region also covered glass beneath the fine indialite microliths (a peak ~480 cm⁻¹). The indialite spectra show a single scattering peak at ~570 cm⁻¹ in the 500–600 cm⁻¹ range, which is typical of high-temperature hexagonal modifications of Mg-Fe-cordierite. Figure 15*b* also shows for comparison the spectra of disordered hexagonal and ordered orthorhombic modifications of synthetic Mg-Fe-cordierite (after Haefeker *et al.*, 2012) and RRUF (100150, <http://rruff.info>), a natural cordierite sample. The hexagonal to orthorhombic transition from indialite to cordierite shows up as an increasing number of Raman scattering peaks from 10 to 33, peak sharpening accompanied by intensity increase, and splitting of the strong band at 567 cm⁻¹ into three bands at 557, 564 and 578 cm⁻¹ (McMillan *et al.* 1984; Poon *et al.*, 1990; Haefeker *et al.*, 2012).

The identification of indialite from Raman spectra agrees with X-ray diffraction analysis of powdered clinkers and paralavas with clinker xenoliths showing a distortion index for this

TABLE 3. Compositions (SEM EDS) for accessory minerals in paralavas from the Nyalga combustion metamorphic complex.

Sample (N)	MN-1127			MN-1129			MN-1133			MN-1176			MN-1193						
	(1)	(2)	(3)	(1)	(4)	(5)	(1)	(7)	(8)	(1)	(6)	(1)	(10)	(11)	(12)	(13)	(14)	(15)	(16)
Analysis	1	2	3	4	5	6	7	8	9	10	11	12	13	14	15	16			
SiO ₂	52.24	44.93			1.37	49.02	32.80	23.58	24.72			24.82	40.46	40.97	38.06				
TiO ₂				8.37	23.22		17.11		0.08										
Al ₂ O ₃	21.56	24.15		2.65	7.22	33.42	25.39		11.33			11.42	32.62	33.15	30.27	58.59			
FeO	0.57	0.82	0.94	74.22	68.43	7.67		0.89	3.40	1.93	1.22	2.83	0.70	1.43	0.55	0.66			
MgO				0.35		8.51													
MnO				1.46	0.53														
CaO	0.62	1.02					0.41	1.11	38.46	0.73	0.91	41.57	2.05	2.47	1.08	39.94			
Na ₂ O	0.84	1.02					0.17		0.69			0.37	12.34	13.19	1.02				
K ₂ O	11.43	5.65				1.11	0.25						8.66	7.22	28.75				
BaO	7.97	21.10	44.65				41.03	57.77		35.71	7.01								
StrO	2.84	15.67	15.67					1.38		22.73	47.53								
SO ₃			38.48							37.43	42.73								
Total	98.07	98.70	90.72	87.04	100.76	99.72	99.88	101.84	78.75	98.53	99.40	81.38	96.84	98.42	99.73	100.17			

(N) – Quantity of analyses. All Fe is expressed as FeO. Blank in analysis are below SEM EDS detection limits. Analysis: 1 – Ba-orthoclase, 2 – hyalophane, 3 and 10 – Sr-rich baryte, 4 – Al-magnetite, 5 – Al-rich, 6 – indialite, 7 – celsian, 8 – fersnoite, 9 and 12 – Al- and Fe-rich tobermorite-like X-mineral, best fit crystal chemical formula: Ca₃Si₃(Al,Fe)(OH)O₁₂·8H₂O. 11 – celestine, 13 and 14 – nepheline, 15 – kalsilite, 16 – perovskite.

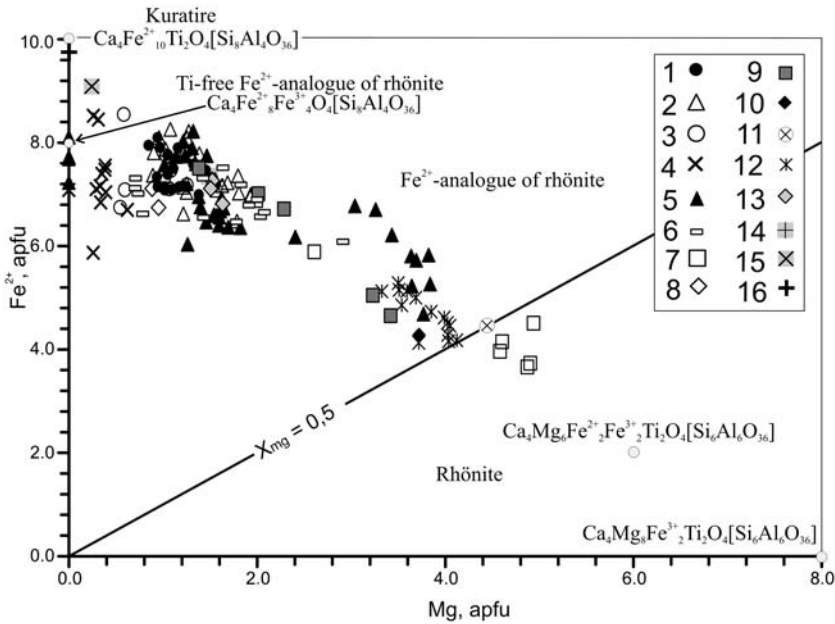


FIG. 9. Minerals of the rhönite–kuratite series from paralavas, terrestrial basaltic rocks and extraterrestrial occurrences in a Fe^{2+} vs. Mg diagram. Formulas are based on 28 cations and 40 oxygens. Symbols refer to samples MN-1127 (1), MN-1287 (2), MN-1128 (3), MN-1129 (4), MN-1133 (5), MN-1175 (6), MN-1176 (7) and MN-1193 (8); other numbers refer to data of Havette *et al.* (1982) (9), Olsson (1983) (10), Gamble and Kyle (1987) (11), Grapes and Keller (2010) (12), Žaček *et al.* (2015) (13), Kuehner and Irving (2007) (14), Treiman (2008) (15) and Hwang *et al.* (2014) (16).

mineral to be $\Delta = 0$, typical of the disordered hexagonal polymorph of Mg-Fe-cordierite.

Sample MN-1133 from the Camel outlier (Fig. 2*b*) is a massive fine-grained paralava (Table 1, an. 10) containing melilite, Al-clinopyroxene and bytownite (An_{90-85}) microphenocrysts (Figs 4–6*a*). Melilites and Al-clinopyroxenes enclose euhedral spinel with $Fe^{2+}/(Mg+Fe^{2+}) = 0.04–0.33$ (Fig. 8). The interstitial phases include nepheline, kirschsteinite microliths and dendritic crystals with inclusions of Ca-bearing fayalite and microliths of Ca-bearing fayalite with, or without, inclusions of kirschsteinite (Figs 7 and 14*a,c,d*), as well as pyrrhotite globules and segregations of celsian (Figs 6*b*, 14*e,f* Table 3, an. 7). Nepheline, fayalite and acicular celsian commonly coexist with an anisotropic phase (hereafter referred to as X-mineral) within the matrix (Fig. 14*a*). The X-mineral has a ~20 wt.% deficit of totals (Table 3, an. 9) and the best fit is the crystal chemical formula $Ca_5Si_3(Al, Fe)(OH)O_{12} \cdot 8H_2O$; it is the most proximal to Al- and Fe-rich tobermorite $Ca_5Si_5(Al, Fe)(OH)O_{16} \cdot 5H_2O$.

The matrix also encloses (from a few micrometres to 70–100 μm in size) globules and round

segregations of a compositionally unusual calcite with 1–2 wt.% SrO, 1–3 wt.% SO_3 and $\pm SiO_2$ (0.1–0.3 wt.%). Segregations of such calcite appear in melilite and Al-clinopyroxene microphenocrysts and may be melt inclusions (Fig. 14*b*) entrapped during crystallization of minerals in the paralava melts, judging by their morphology. Typically they occur in interstices between microphenocrysts and are surrounded with fayalite and nepheline (Fig. 14*c,d*), sometimes filling almost the entire interstitial space.

Other interstitial phases are elongate crystals or microliths of kuratite ($X_{Mg} = 0.013–0.20$; Table 2, an. 8, 9), as well as sporadic microliths of a phase similar to the Ti-free Fe^{2+} -analogue of rhönite (Table 2, an. 10). The sample contains a few round pyrrhotite segregations, up to 1 cm across, which are cut by magnetite veinlets and enclose drop-shaped inclusions of native iron. Some 30–50 μm vesicles within the pyrrhotite segregations are filled with Sr-rich baryte or celestine (Table 3, an. 10, 11). The matrix also includes aggregates of goethite, siderite and calcite, as well as up to 1.5 mm xenogenic segregations consisting of micrometre-

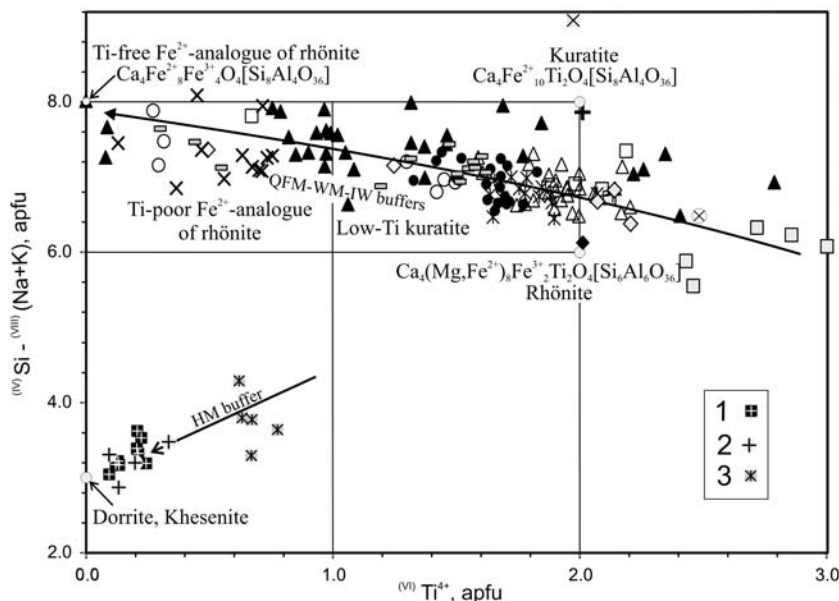


FIG. 10. Minerals of the rhönite–kuratite series and Fe³⁺-rich phases close to the dorrite and khesenite end-members in (IV)Si - (VIII)(Na+K) vs. (VI)Ti⁴⁺ diagram for the sapphirine supergroup. Symbols refer to data of Cosca *et al.* (1988) (1), Foit *et al.* (1987) (2), Havette *et al.* (1982) (3). Other symbols same as in Fig. 9.

sized calcite, goethite, pyrrhotite, and chlorite surrounded by a layer of monticellite with a melilite rim.

There are melilite-celsian segregations, up to 1 mm across (Fig. 14e), containing few crystals of Mg-rich kuratite ($X_{\text{Mg}} = 0.28\text{--}0.45$; Table 2, an. 7), one with an inclusion of celsian; the interstices between celsian and melilite crystals host round pyrrhotite and up to 3–4 μm microliths of fresnoite $\text{Ba}_2\text{TiSi}_2\text{O}_8$ (Fig. 14f; Table 3, an. 8).

Sample MN-1176 from the Camel outlier (Fig. 2b) is a massive fine-grained paralava with a matrix of melilite and Al-clinopyroxene microphenocrysts (Figs 4 and 5), occasionally with crystals of anorthite (An_{99-97}) (Fig. 6a) and spinel with $\text{Fe}^{2+}/(\text{Mg}+\text{Fe}^{2+}) = 0.10\text{--}0.24$ (Fig. 8), both growing into the rims of Al-clinopyroxenes. The interstitial phases are nepheline (Table 3, an. 13), Al- and Fe-rich tobermorite-like X-mineral, pyrrhotite and palagonite aggregate. Nepheline encloses numerous subparallel oriented elongate dendritic crystals of Ca-bearing fayalite with kirschsteinite inclusions (Figs 7 and 13e). The segregations of the X-mineral (Table 3, an. 12) are quite abundant (Fig. 13e), as well as pyrrhotite globules with inclusions of native iron (Fig. 13f); the palagonite aggregate shows strongly variable

contents of Si, Fe, Mg and Ca with a 20–30 wt.% of deficit in totals.

The sample contains 2 mm \times 4 mm vesicles lined with successive layers of calcite, palagonite aggregate and pyrrhotite overgrown with perovskite microliths. There are also xenogenic segregations, 2–3 mm across, composed of fine calcite, goethite, melilite, perovskite, monticellite and pyrrhotite. Melilites in these segregations have compositions unusual for paralavas, intermediate between the äkermanite and gehlenite + ferrigehlenite end-members, with minor FeO of 1–3.5 wt.% (Fig. 4).

Rhönite crystals coexist with Ca- and Mg-bearing fayalite microliths in interstitial nepheline and contain approximately equal amounts of Mg and Fe²⁺ ($X_{\text{Mg}} = 0.52\text{--}0.57$; Fig. 9). One rhönite microlith has a 3–4 μm thick rim corresponding to Ti-poor Fe²⁺-analogue of rhönite ($X_{\text{Mg}} = 0.31$), with 3.3 wt.% TiO₂, which is lower than the 10–11 wt.% average for rhönite microlith (Table 2, an. 13, 14).

Sample MN-1193 from the vicinity of Camel outlier is a massive fine-grained paralava, different from the other samples in the presence of interstitial kalsilite coexisting with nepheline (Table 3, an. 14, 15). Microliths of anorthite (An_{100-90}) occur as inclusions in Al-clinopyroxene and melilite

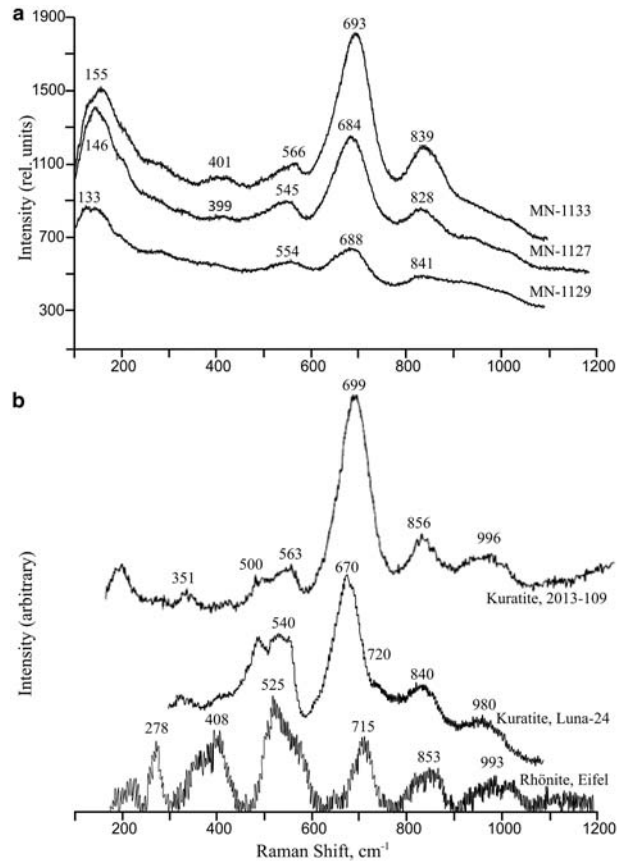


FIG. 11. Raman scattering spectrum of the rhönite–kuratite series minerals in Nyalga paralavas (a), compared with the spectra (b) of extraterrestrial kuratites 2013-109, Luna 24 regolith, and terrestrial rhönite, RRUF spectra 060316 (Eifel), unoriented grains, 532 nm excitation.

microphenocrysts (Figs 4–6a). Anorthite apparently crystallized first from the paralava melt. The sample bears xenogenic segregations, up to 3 mm × 4 mm across, composed of fine-grained aggregates of melilite, Ca-bearing (up to 3 wt.% CaO) forsterite, perovskite (Table 3, an. 16), pyrrhotite globules and palagonite aggregate. Nepheline and kalsilite enclose microliths of kirshtenenite with inclusions of Ca-bearing fayalite, as well as celsian, Mg-rich hercynite and pyrrhotite globules. Low-Ti kuratite and Ti-poor Fe²⁺-analogue of rhönite ($X_{Mg} = 0.11–0.12$; Table 2, an. 15, 16) occurs as microliths.

Discussion

Judging by the mineral assemblages, the microliths of spinel – Fe-rich spinel and anorthite–bytownite

crystals were the first to crystallize in the Nyalga paralava melts, and were followed by microphenocrysts of Al-clinopyroxene, melilite ± Mg-Fe olivine (hortonolite). The minerals of the rhönite–kuratite series formed after early microphenocrysts. Crystals and microliths of kuratite, rhönite, low-Ti kuratite and Ti-poor Fe²⁺-analogue of rhönite crystallized in microphenocrysts interstices from residual Si-Al-K and Si-Al-Ca-Fe immiscible melts together with Fe³⁺-bearing hercynite, Ca-bearing fayalite, kirschsteinite, pyrrhotite ± native iron, wüstite, magnetite, celsian, hyalophane, Ba-orthoclase, fresnoite and before nepheline ± kalsilite and later phases of calcite, siderite, Sr-rich baryte, baryte, celestine and gypsum.

The round segregations of calcite found in some paralava samples (MN-1133 and others) inside melilite and Al-clinopyroxene microphenocrysts

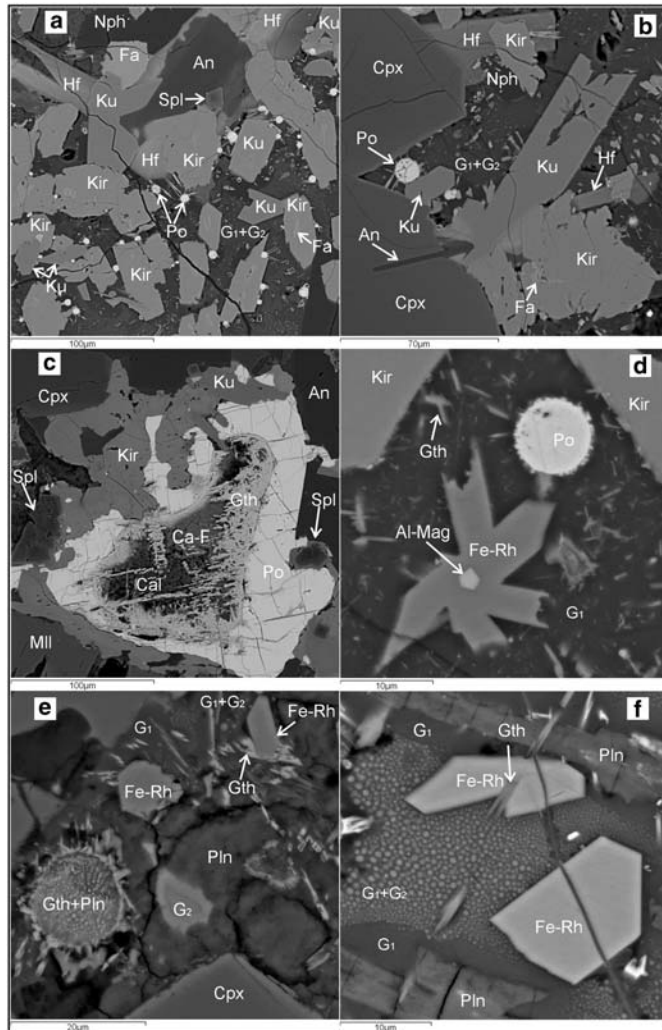


FIG. 12. Back-scatter electron (BSE) images illustrating phase relations among minerals of the rhönite–kuratite series in paralavas. (a) Sample MN-1127: kirschsteinite microliths with inclusions of Ca-bearing fayalite, and few kuratite microliths in Si-Al-K and Si-Al-Ca-Fe glasses (microemulsion of quenched melts), all in interstices between microphenocrysts. Glasses, in turn, enclose goethite needles and small pyrrhotite globules. Hyalophane grows over anorthite. (b) Sample MN-1127: hyalophane and kirschsteinite microliths and euhedral kuratite crystals growing over Al-clinopyroxene microphenocrysts. Si-Al-K glass encloses numerous globules (droplets) of sub-micrometre and μ m-sized Si-Al-Ca-Fe glasses, kirschsteinite microliths with Ca-bearing fayalite inclusions, pyrrhotite globules and goethite needles. (c) Sample MN-1287: zoned segregation with a pyrrhotite margin, which encloses a kuratite crystal and kirschsteinite microliths, around an aggregate of acicular goethites and an oxygen-rich Ca-F phase similar to fluorite, and calcite. (d) Sample MN-1128: euhedral crystals of a Ti-poor Fe^{2+} -analogue of rhönite with Al-magnetite inclusions in Si-Al-K glass containing a pyrrhotite globule and numerous fine goethite needles. (e) Sample MN-1129: crystal and microlith of the Ti-poor Fe^{2+} -analogue of rhönite in Si-Al-K glass, a palagonite aggregate which replaces Si-Al-Ca-Fe glass, and goethite. (f) Sample MN-1129: euhedral crystals of Ti-poor Fe^{2+} -analogue of rhönite in two glasses (microemulsion of quenched Si-Al-K and Si-Al-Ca-Fe immiscible melts). Mineral names are abbreviated as Fa = Ca-bearing fayalite, Hf = hyalophane, Po = pyrrhotite, Fe-Rh = Ti-poor Fe^{2+} -analogue of rhönite, Gth = goethite, Al-Mag = Al-magnetite, Ca-F = oxygen-rich Ca-F phase, Cal = calcite, G_1 = Si-Al-K glass, G_2 = Si-Al-Ca-Fe glass, and Pln = palagonite aggregate. Other symbols are the same as in Fig. 3.

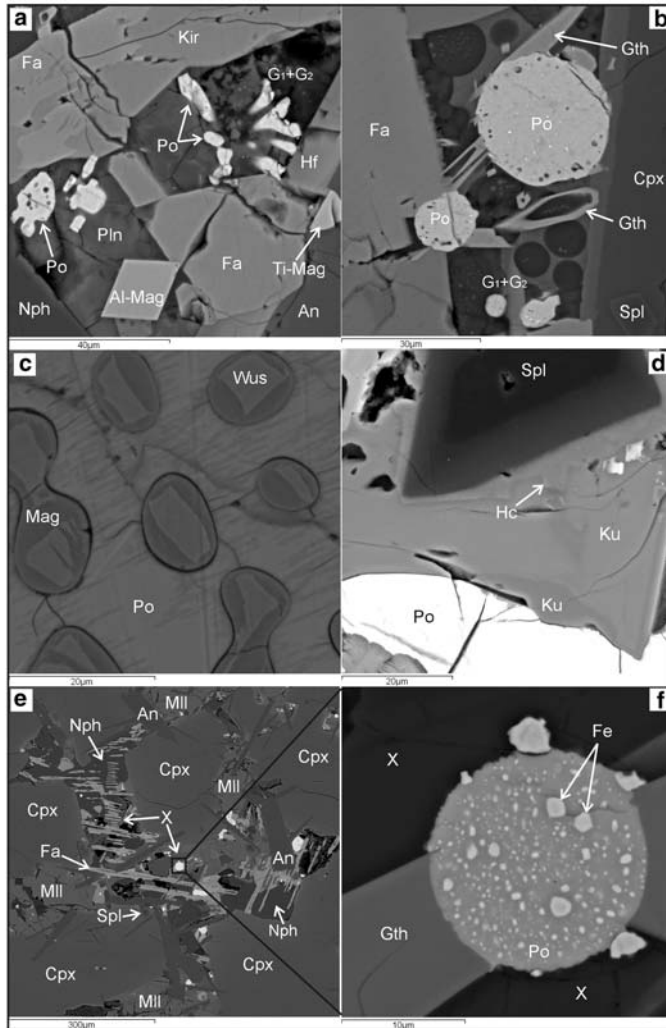


FIG. 13. BSE images illustrating phase assemblages of paralavas containing minerals of the rhönite–kuratite series. (a) Sample MN-1127: palagonite aggregate, nepheline, and residual glasses among microliths of Ca-bearing fayalite, kirschsteinite with Ca-bearing fayalite isolations, Al-magnetite, titanium magnetite, hyalophane and pyrrhotite. (b) Sample MN-1127: two glasses with inclusions of acicular and hopper crystals of goethite, pyrrhotite globules between a microlith of Ca-bearing fayalite and an Al-clinopyroxene micropenocryst. (c) Sample MN-1287: drop-shaped inclusions of a wüstite precursor to magnetite, in a pyrrhotite segregation. (d) Sample MN-1287: kuratite-pyrrhotite contact; kuratite growing over a zoned iron-rich spinel crystal with a hercynite rim. (e) Sample MN-1176: interstitial nepheline which encloses numerous subparallel oriented elongate dendritic crystals of Ca-bearing fayalite, zoned spinel crystals, pyrrhotite globules and segregations of tobermorite-like X-mineral. (f) Sample MN-1176: X-mineral which encloses a pyrrhotite globule containing inclusions of native iron intergrown with a goethite crystal, enlarged from (e). Mineral names are abbreviated as Mag = magnetite, Wus = wüstite, Hc = hercynite, Cls = celsian, Fsn = fresnoite, Fe = native iron, Ti-Mag = titanium magnetite, X = Al- and Fe-rich tobermorite-like X-mineral. Other symbols same as in Figs 3 and 12.

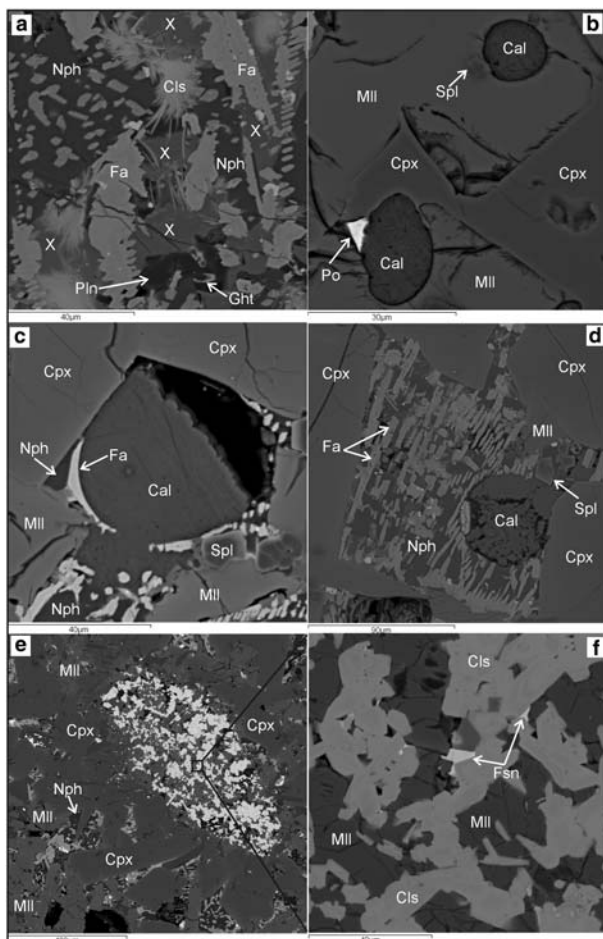


FIG. 14. BSE images of phase assemblages in paralava samples MN-1133. (a) Nepheline filling interstices between microphenocrysts, with inclusions of Ca-bearing fayalite, celsian, tobermorite-like X-mineral, and palagonite aggregate enclosing goethite; (b) melt inclusions of calcite in melilite and Al-clinopyroxene microphenocrysts; (c) calcite globule (quenched calcitic melt?) rimmed by Ca-bearing fayalite between Al-clinopyroxene and melilite microphenocrysts; (d) calcite globule surrounded by nepheline-fayalite aggregate and spinel crystals between Al-clinopyroxene microphenocrysts; (e) melilite-celsian segregation in paralava matrix; (f) melilite-celsian segregation with fresnoite (Fsn) microliths, enlarged from (e); Symbols are the same as in Figs 3, 12 and 13.

(Fig. 14b), interpreted as melt inclusions, suggest that drops of carbonate (calcitic) melt may have existed within silicate melt when the microphenocrysts were crystallizing. Such calcite segregations probably formed after quenching and crystallization of the calcitic melt as the earliest carbonate phases in paralavas. Note that, according to experimental evidence, calcitic melt can result from melting of calcite or calcitic-bearing rocks at temperatures above 650–700°C and a pressure of 1 kbar (Durand *et al.*, 2015 and references therein).

During the formation of the Nyalga paralavas, carbonate-silicate sediments underwent melting and decarbonation at temperatures above 1100°C (see below), but at a nearly ambient pressure. Low-pressure and high-temperature changes in carbonate-silicate sedimentary rocks, leading to the formation of a calcitic melt in paralavas, remain unclear and require further investigation.

Analytical data indicate that residual Si-Al-K (Table 1, an. 2, 5, 6, 8) and Si-Al-Ca-Fe glasses may contain water. The presence of water may be due

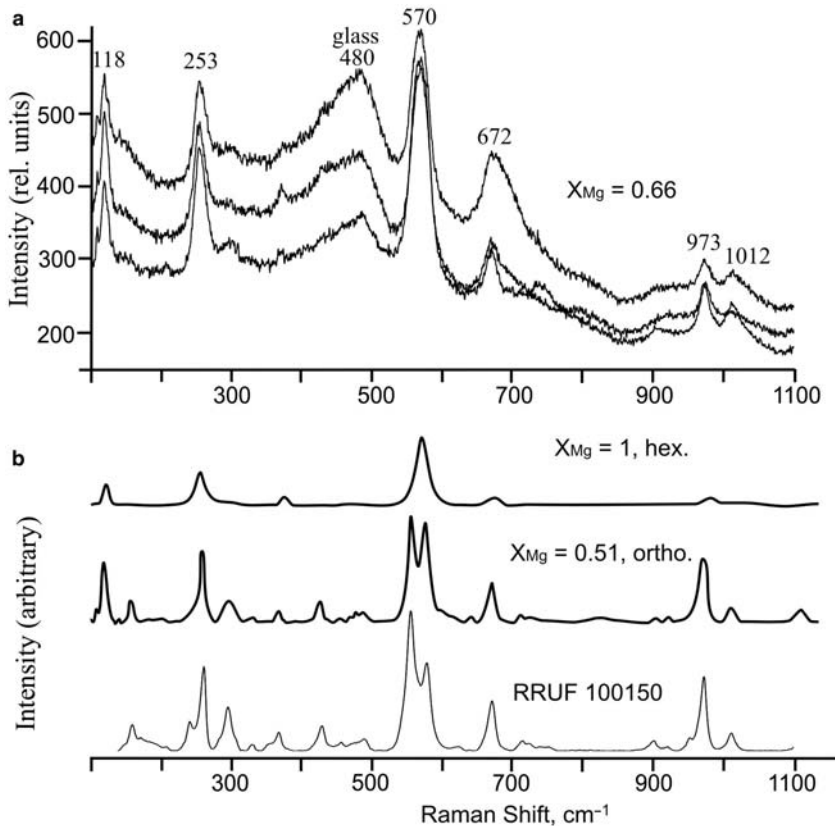


FIG. 15. Raman scattering spectrum of indialite crystals: (a) in glass of a clinker xenolith from paralava sample MN-1129, compared with the spectra (b) of synthetic hexagonal and orthorhombic modifications of Mg-Fe-cordierite (Haefeker *et al.*, 2012) and cordierite RRUF spectra 100150, unoriented grains, 532 nm excitation.

either to high water contents in residual melts that remained in interstices between microphenocrysts after more than 95 wt.% anhydrous mineral crystallization in the paralavas or to supergene hydration of glasses during erosion of sediments for millions of years at the formation of the outliers (Fig. 2). The former explanation is consistent with the observation that secondary alteration signatures occur inside, or near, glasses in fresh paralava samples. Dacitic glass in clinker xenoliths (Table 1, an. 9) and mottles of Al-rich glass (Table 1, an. 3, 7) in the paralava matrix have totals approaching 98 wt.% and are anhydrous or contain only minor amounts of water. These compositions of glasses, as well as sporadic distribution of altered zones in the paralavas, are not consistent with supergene alteration which typically spreads all over the rocks irrespective of the location of residual Si-Al-K and Si-Al-Ca-Fe glasses.

Goethite is only found inside residual glasses and the palagonite aggregate (Figs 12, 13*b* and 14*a*), whereas the segregations of an Al- and Fe-bearing tobermorite-like X-mineral occur in their vicinity (Figs 13*e* and 14*a*). Goethite and the hydrous X-mineral possibly crystallized in the presence of the fluid phase during devitrification of residual glasses at low temperatures while the paralavas were cooling. Otherwise, goethite may have replaced Al-magnetite under the effect of highly alkaline fluid (pH~13) through dissolution/crystallization reactions with the formation of intermediate maghemite (He and Traina, 2007). The high alkalinity of the fluid released during devitrification of residual glasses may be due to concentration of K₂O as high as 10–13 wt.% (Table 1, an. 2, 5, 6, 8). Note also that tobermorite and tobermorite-like minerals are typical low-temperature ‘cement’ phases (Richardson, 2004).

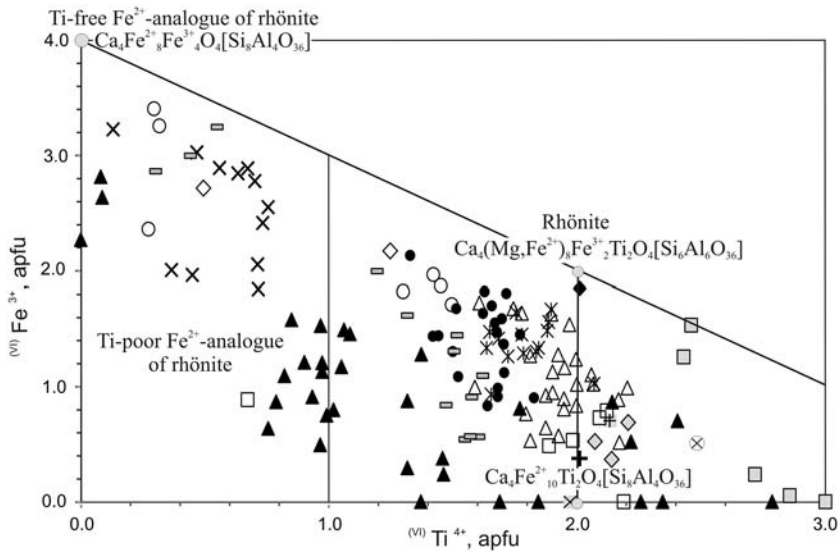


FIG. 16. Minerals of the rhönite–kuratite series in paralavas, terrestrial basaltic rocks and extraterrestrial occurrences in a $(\text{VI})\text{Ti}^{4+}$ vs. $(\text{VI})\text{Fe}^{3+}$ diagram. Symbols are the same as in Fig. 9.

The residual glasses were apparently replaced by the palagonite aggregate in supergene conditions.

In terrestrial conditions, rhönite crystallizes from silica-undersaturated mafic alkaline melts with a CIPW-norm ratio of $\text{Ne}/(\text{Ne}+\text{Ab}+\text{Or}+\text{Lc}) > 0.18$ and an X_{Mg} value of $\text{MgO}/(\text{MgO}+\text{FeO}+\text{Fe}_2\text{O}_3) > 0.46$ (Kunzmann, 1999). The kuratite- and rhönite-bearing paralavas from the Nyalga combustion metamorphic complex meet these criteria with $\text{Ne}/(\text{Ne}+\text{Lc}) = 0.23\text{--}0.76$ (zero Ab and Or norms) and $X_{\text{Mg}} = 0.48\text{--}0.71$ (Table 1). At the atmospheric pressure, the assemblage of rhönite + olivine + clinopyroxene + plagioclase microphenocrysts in basanitic melts is stable over a narrow temperature range between 1082 and 1100°C and at oxygen fugacity (f_{O_2}) about the IW (without magnetite) and NNO (with magnetite) buffers (Boivin, 1980). According to experimental and modelling data for the Kaiserstuhl tephrite and limburgite (Grapes and Keller, 2010), the Fe^{2+} -analogue of rhönite crystallizes together with olivine, clinopyroxene and plagioclase at 1068 to 1137°C, <50 bar, and a f_{O_2} about the QFM buffer.

The paralava samples studied are similar in bulk composition (Table 1) but differ significantly in mineral assemblages. Minerals of the rhönite–kuratite series differ in percentages and compositions both between and within the samples. Paralavas contain these minerals in various combinations depending on bulk Mg contents in rocks.

Namely, rhönite and Mg-rich kuratite occur in samples MN-1133, MN-1171 and MN-1174 with $X_{\text{Mg}} = 0.60\text{--}0.71$ from the Camel outlier, while kuratite and low-Ti kuratite are present in Crown outlier samples MN-1127 and MN-1287 with $X_{\text{Mg}} = 0.48\text{--}0.53$ (Table 1).

Kuratite and rhönite commonly coexist with Mg-Fe and Fe-Ca olivines which have strongly variable percentages of the Mg_2SiO_4 , CaMgSiO_4 , Fe_2SiO_4 and CaFeSiO_4 end-members (Fig. 7). The samples contain Mg-Fe olivine (hortonolite) microphenocrysts, as well as Ca-bearing fayalite microliths without kirshtenenite inclusions and kirshtenenite microliths without fayalite inclusions (Figs 12a,c, 13a and 14a). These olivines apparently remain homogeneous after crystallization due to rapid cooling to 850°C, below which cation exchange in the Mg-Fe-Ca olivine solid solution is impossible (Mukhopadhyay and Lindsley, 1983). However, most olivine microliths host different volume fractions of Ca-bearing fayalite or kirshtenenite inclusions (Figs 12a,b and 13a) and apparently result from exsolution of Fe-Ca olivines during the cooling of paralavas. As shown by experimental data of Mukhopadhyay and Lindsley (1983), olivine solid solutions of compositions intermediate between fayalite and kirschsteinite exsolve at temperatures from 1150 to 850°C. The olivine compositions plot near the Fe_2SiO_4 – CaFeSiO_4 side of the ternary diagram of Fig. 7, in

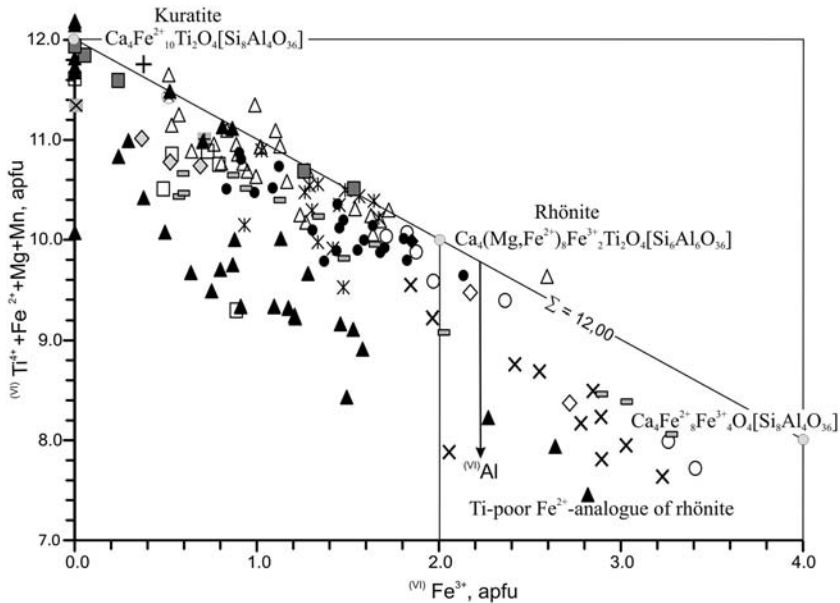


FIG. 17. Minerals of the rhönite–kuratite series in paralavas, terrestrial basaltic rocks and extraterrestrial occurrences in $(^{VI})\text{Ti}^{4+} + \text{Fe}^{2+} + \text{Mg} + \text{Mn}$ vs. $(^{VI})\text{Fe}^{3+}$ diagram. Compositions plot away from the $\Sigma = 12.00$ line in the presence of $(^{VI})\text{Al}$ along with $(^{VI})\text{Fe}^{3+}$. Symbols are the same as in Fig. 9.

accordance with the experimentally determined surface solvus (Davidson and Mukhopadhyay, 1984), most typically at temperatures of 1000–800°C. The exsolution of Ca-bearing fayalite and kirschsteinite from homogeneous Fe–Ca olivine solid solution possibly postdates the crystallization of rhönite–kuratite series minerals. Note also that the coexistence of Ca-bearing fayalite and kirschsteinite is extremely rare in terrestrial magmatic rocks and natural combustion metamorphic melt rocks. To date, such unusual olivines have only been described in the lavas of Colli Albani volcano, Italy (Melluso *et al.*, 2010), meteorites and technogenic paralavas from burned spoil-heaps, South Urals, Russia (Sokol *et al.*, 2002).

The presence of newly-formed crystals of indialite (high-temperature hexagonal polymorph of cordierite, Fig. 15a) in glasses of partially molten clinker xenoliths from samples MN-1128 and MN-1129 provides evidence that paralava minerals crystallized at temperatures above 900–1000°C, because crystallization at lower temperatures instead would have produced orthorhombic cordierite (Haefeker *et al.*, 2012). Indialite contains up to 0.3 apfu K at 2.3 wt.% K₂O and is a rare potassic variety, which is a stable phase typical of

high-temperature metamorphic environments of sanidine facies at very low pressures (Schreyer *et al.*, 1990). For instance, potassic indialite in xenolithic ejecta of Somma-Vesuvius formed at a shallow depth and a maximum temperature $\approx 1200^\circ\text{C}$ (Balassone *et al.*, 2004). Indialite has preserved its hexagonal structure possibly due to very rapid cooling during crystallization and melt quenching in clinker xenoliths.

Thus, the minerals of the rhönite–kuratite series in the Nyalga paralava samples belong to mineral assemblages implying crystallization at high temperatures, which are inferred to be $\sim 1100^\circ\text{C}$ by analogy with the experimentally determined (Boivin, 1980) and calculated (Grapes and Keller, 2010) temperatures of rhönite formation.

The Nyalga complex results from local melting of mud rocks and decarbonation reactions during melting of iron-bearing carbonate-silicate sediments maintained by heat conduction from burning coal at nearly atmospheric pressures. The conditions of melting and crystallization were strongly reducing (f_{O_2} at IW and MW buffers), judging by bulk paralava compositions with FeO/Fe₂O₃ molar ratios from 9 to 44 (Table 1) and mineral assemblages that include minerals of the rhönite–kuratite series in association with

pyrrhotite containing drop-shaped native iron inclusions (Fig. 13f), as well as wüstite partially replaced by magnetite (Fig. 13c).

The Fe³⁺-bearing low-Ti variety of kuratite and Ti-poor Fe²⁺-analogue of rhönite crystallized later than kuratite and rhönite, together with titanium magnetite, Al-magnetite and Fe³⁺-bearing hercynite (Fig. 13a,d), under higher oxygen fugacity, probably between MW and QFM buffers. They crystallized in the Si-Al-K melt or in a microemulsion of immiscible Si-Al-K and Si-Al-Ca-Fe melts (Figs 12b,f and 13b) containing <0.1 wt.% Ti (Table 1, an. 5, 6). Low Ti contents in the residual silicate melts can be partly due to mixing of the mafic paralava melts with the material of molten Al-rich clinker xenoliths compositionally proximal to dacite.

A gradual decrease in Ti and Mg with increasing Fe³⁺ and Si in the rims of microliths or in crystals of minerals in the rhönite–kuratite series indicates the existence of a continuous series of compositions between kuratite Ca₄Fe₁₀²⁺Ti₂O₄[Si₈Al₄O₃₆] and rhönite Ca₄(Mg,Fe²⁺)₈Fe₂³⁺Ti₂O₄[Si₆Al₆O₃₆] to Ti-free Fe²⁺-analogue of rhönite Ca₄Fe₈²⁺Fe₃³⁺O₄[Si₈Al₄O₃₆] (Figs 10, 16 and 17). Isomorphic substitution in this series, which includes all known compositions of the Fe²⁺-dominant variety of rhönite-subgroup minerals from terrestrial rocks, occurs by the cation exchange reaction Mg²⁺ + 2Ti⁴⁺ ↔ Si⁴⁺ + 2Fe³⁺ (Fig. 10). The contents of Al, Fe²⁺ and Ca vary insignificantly and irregularly. Large deviations from the Σ_{VI} = 12.00 line indicates the presence of ^{VI}Al reaching 2 apfu in Ti-poor Fe²⁺-dominant minerals of the rhönite–kuratite series (Table 2; Fig. 17).

The Fe²⁺ concentrations are the highest (7.2–8.0 apfu; Fig. 7; Table 2) in terrestrial kuratites from the paralavas in the Choir–Nyalga basin, as well as those found in the Most basin of the Czech Republic (Žaček *et al.*, 2015), and in alkali basalts intruding corals in Réunion Island (Havette *et al.*, 1982). Kuratites from the Réunion basalts have Ti as high as 2.4–3.0 apfu. Kuratites in these terrestrial occurrences have higher Al, Ca concentrations than the Fe²⁺-analogue of rhönite from the Kaiserstuhl volcanic complex (Grapes and Keller, 2010), and the lowest Na impurity. Extraterrestrial kuratites from the angrite meteorite (Hwang *et al.*, 2014, 2016) and Luna 24 regolith (Treiman, 2008) have the highest content of Si (8 and 9 apfu respectively, Fig. 10).

The formation conditions of the rhönite–kuratite series minerals from terrestrial and extraterrestrial occurrences were different from those for Fe³⁺-dominant varieties of rhönite subgroup (dorrite

and khesinite) in terms of oxygen fugacity. Dorrite, Ca₄(Mg₃Fe₉³⁺)O₄[Si₃Al₈Fe₃³⁺O₃₆] (Cosca *et al.*, 1988) and khesinite, Ca₄(Mg₃Fe₉³⁺)O₄(Fe₉³⁺Si₃)O₃₆ (Galuskina *et al.*, 2014) are extreme end-members in a series of compositions with increasing Fe³⁺ but decreasing Ti, Si and Al in the classification diagram of sapphirine-supergroup minerals (Fig. 10). The rhönite-subgroup minerals with the highest Fe³⁺ are stable at high oxygen fugacity, high temperatures and low pressures and occur in combustion metamorphic or pyrometamorphic melt rocks (Foit *et al.*, 1987; Cosca *et al.*, 1988; Chesnokov *et al.*, 1994; Galuskina *et al.*, 2014), as well as at contacts between alkali basalts and corals (Havette *et al.*, 1982). The *f*_{O₂} conditions inferred for crystallization of dorrite from the Wyoming paralava are as high as the hematite-magnetite buffer (Cosca *et al.*, 1988). Thus, the Fe-rich varieties of rhönite-subgroup minerals form at high temperatures and very low pressures but in different redox conditions: low *f*_{O₂} (IW-WM-QFM buffers) for minerals of the rhönite–kuratite series and high *f*_{O₂} (HM buffer) for minerals compositionally similar to the dorrite–khesinite series.

The minerals of the rhönite–kuratite series commonly coexist with Ca-clinopyroxene (Al-rich diopside–hedenbergites) and spinel-group minerals (spinel, hercynite, titanium magnetite, Al-magnetite). In terms of crystal structure, rhönite is a chain silicate with alternating ‘pyroxene’ and ‘spinel’ slabs (Bonaccorsi *et al.*, 1990). This structural feature may be responsible for the limited stability field of rhönite in a narrow temperature range (Sharigin *et al.*, 2011). The conditions in which minerals of the rhönite–kuratite series can form have multiple controls: crystal structure, temperature, melt composition, and others, such as melt cooling rate. As a result, either Al-clinopyroxene and spinel-group minerals or rhönite, kuratite, low-Ti kuratite and Ti-poor Fe²⁺-analogue of rhönite can crystallize depending on minor local changes in the compositions of silica-undersaturated mafic melts, temperature, oxygen fugacity, and the rate of cooling during the crystallization of paralavas.

Implications and conclusions

Minerals of the rhönite–kuratite series in the Nyalga paralavas crystallized after spinel-group minerals, plagioclase, melilite, Al-clinopyroxene ± Mg-Fe olivine in residual Si-Al-K and Si-Al-Ca-Fe immiscible melts. Kuratite, rhönite and the Ti-poor

Fe²⁺-analogue of rhönite crystallized together with rare phases (Ca-bearing fayalite, kirschsteinite, K-Ba feldspars and fresnoite) before nepheline ± kalsilite, carbonates and sulfates. Goethite and a tobermorite-like X-mineral formed in interstices of microphenocrysts during cooling of paralavas at low temperatures by devitrification of residual glasses and replacement reactions. Most crystals and microliths of the rhönite–kuratite series have intermediate compositions between kuratite, rhönite and a Ti-poor mineral which approaches the unnamed Ti-free Fe²⁺-analogue of rhönite.

Minerals of the rhönite–kuratite series crystallized at temperatures ≈1100°C from melts with bulk compositions of X_{Mg} ≈ 0.5 and Ne/(Ne+Lc) = 0.23–0.76. The diversity of mineral assemblages in the paralava samples is due to local composition variations of silica-undersaturated Ca-rich mafic melts which were produced by melting of iron-bearing carbonate-silicate sediments at low oxygen fugacity about the IW-WM-QFM buffers and at nearly atmospheric pressure, in the vicinity of burning coal beds.

The limited occurrence of the rhönite–kuratite series minerals in natural terrestrial rocks (seven sites) suggests that the combination of *P-T-X* conditions favourable for kuratite crystallization from mafic melts can rarely happen during terrestrial magmatism and combustion metamorphism. New finds of these rare minerals can be expected from terrestrial combustion metamorphic, pyrometamorphic or extraterrestrial rocks that result from crystallization of silica-undersaturated iron-bearing silicate mafic melts in strongly reducing conditions at high temperatures and very low pressures.

There remains a lot to learn about the exceptionally diverse mineralogy of melt rocks of the Nyalga complex in the Choir–Nyalga basin. Further studies of these melt rocks, which have no known counterparts, will focus on the properties of rare and new minerals (Ti-free Fe²⁺-analogue of rhönite, indialite–ferroindialite series, tobermorite-like X-mineral, plus others); melting processes of mud rocks and silicate-carbonate sediments which produced compositionally heterogeneous silicate and other melts (silicate, metal iron, calcite and sulfide); origin of calcitic melt and immiscibility of melts; geochemistry and isotopic characteristics of clinkers and paralavas.

Acknowledgements

We are grateful to Ellina Sokol for constructive criticism and valuable advice. The comments of the

anonymous reviewer on the mineral nomenclature and chemistry helped to improve the manuscript. The study was supported by grant 16-05-00518 from the Russian Foundation of Basic Research and grant 9638.2016.5 of Scientific School of Russian Federation.

References

- Balassone, G., Franco, E., Mattia, C.F. and Pulity, R. (2004) Indialite in xenolithic rocks from Somma-Vesuvius volcano (Southern Italy): Crystal chemistry and petrogenetic features. *American Mineralogist*, **89**, 1–6.
- Boivin, P. (1980) Données expérimentales préliminaires sur la stabilité de la rhönite à 1 atmosphère. Application aux gisements naturels. *Bulletin de Minéralogie*, **103**, 491–502.
- Bonaccorsi, E., Merlino, S. and Pasero, M. (1990) Rhönite: structure and microstructural features, crystal chemistry and polysomatic relationships. *European Journal of Mineralogy*, **2**, 203–218.
- Chesnokov, B.V., Vilisov, V.A., Bushmakin, A.F., Kotlyarov, V.A. and Belogub, E.B. (1994) New minerals from burned spoil-heaps of the Chelyabinsk coal basin (sixth report) [in Russian, with English Abstr.]. *Uralskiy Mineralogicheskii Sbornik*, **3**, 3–34.
- Cosca, M.A., Rouse, R.R. and Essene, E.J. (1988) Dorrite [Ca₂(Mg,Fe³⁺)(Al₄Si₂)O₂₀], a new member of the aenigmatite group from a pyrometamorphic melt-rock. *American Mineralogist*, **73**, 1440–1448.
- Cosca, M.A., Essene, E.J., Geissman, J.G., Simmons, W. B. and Coates, D.A. (1989) Pyrometamorphic rocks associated with naturally burned coal beds, Powder River Basin, Wyoming. *American Mineralogist*, **74**, 85–100.
- Davidson, P.M. and Mukhopadhyay, D.K. (1984) Ca-Fe-Mg olivines: Phase relations and a solution model. *Contribution to Mineralogy and Petrology*, **86**, 256–263.
- Deer, W.A., Howie, R.A. and Zussman, J. (1992) *An Introduction to the Rock-Forming Minerals*. Longman Scientific & Technical, Harlow, UK.
- Durand, C., Baumgartner, L.P. and Marquer, D. (2015) Low melting temperature for calcite at 1000 bars on the join CaCO₃-H₂O – some geological implications. *Terra Nova*, **27**, 364–369.
- Erdenetsogt, B., Lee, I., Bat-Erdene, D. and Jargal, L. (2009) Mongolian coal-bearing basins: geological settings, coal characteristics, distribution, and resources. *International Journal of Coal Geology*, **80**, 87–104.
- Foit, F.F., Hooper, R.L. and Rosenberg, P.E. (1987) An unusual pyroxene, melilite, and iron oxide mineral assemblage in a coal-fire buchite from

- Buffalo, Wyoming. *American Mineralogist*, **72**, 137–147.
- Galuskina, I.O., Galuskin, E.V., Pakhomova, A.S., Widmer, R., Armbruster, T., Lazic, B., Grew, E.S., Vapnik, Y., Dzierzanowski, P. and Murashko, M. (2014) Khesinite, IMA 2014-033. CNMNC Newsletter No. 21, August 2014, page 802; *Mineralogical Magazine*, **78**, 797–804.
- Gamble, J.G. and Kyle P.R. (1987) The origin of glass and amphibole in spinel wehrlite xenoliths from Foster Crater, McMurdo Volcanic Group, Antarctica. *Journal of Petrology*, **28**, 755–780.
- Grapes, R. and Keller, J. (2010) Fe²⁺-dominant rhönite in undersaturated alkaline basaltic rocks, Kaiserstuhl volcanic complex, Upper Rhine Graben, SW Germany. *European Journal of Mineralogy*, **22**, 285–292.
- Grapes, R.H., Wysoczanski, R.J. and Hoskin, P.W.O. (2003) Rhönite paragenesis in pyroxenite xenoliths, Mount Sidley volcano, Marie Byrd Land, West Antarctica. *Mineralogical Magazine*, **67**, 639–651.
- Grew, E.S., Hälenius, U., Pasero, M. and Barbier, J. (2008) Recommended nomenclature for the sapphirine and surinamite groups (sapphirine supergroup). *Mineralogical Magazine*, **72**, 839–876.
- Grünhagen, H. and Seck, H.A. (1972) Rhönite aus einem Melaphonolith vom Puy de Saint-Sandoux (Auvergne). *Tschermaks Mineralogische und Petrographische Mitteilungen*, **18**, 17–38.
- Haefeker, U., Kaindl, R. and Tropper, P. (2012) Semi-quantitative determination of the Fe/Mg ratio in synthetic cordierite using Raman spectroscopy. *American Mineralogist*, **97**, 1662–1669.
- Haggerty, S.E. (1991) Oxide mineralogy of the upper mantle. Spinel mineral group. Pp. 355–416 in: *Oxide Minerals: Petrologic and Magnetic Significance* (D. H. Lindsley, editor). Reviews in Mineralogy, **Vol. 25**. Mineralogical Society of America.
- Havette, A., Clocchiatti, R., Nativel, P. and Montaggioni, L. (1982) Une paragenèse inhabituelle à fassaïte, mëlilite et rhönite dans un basalte alcalin contaminé au contact d'un récif coralline (Saint-Lieu, Ile de la Réunion). *Bulletin de Minéralogie*, **105**, 364–375.
- He, Y.T. and Traina, S.J. (2007) Transformation of magnetite to goethite under alkaline pH conditions. *Clay Minerals*, **42**, 13–19.
- Hwang, S-L., Shen, P., Chu, H-T., Yui, T-F., Varela, M-E. and Iizuka, Y. (2014) Kuratite (IMA 2013-109): The 'unknown' Fe-Al-Ti silicate from the angrite D'Orbigny (abstract). in: *45th Lunar and Planetary Science Conference*. LPI Contribution no. 1777, 1818.
- Hwang, S-L., Shen, P., Chu, H-T., Yui, T-F., Varela, M-E. and Iizuka, Y. (2016) Kuratite Ca₄(Fe₁₀²⁺Ti₂)O₄[Si₈Al₄O₃₆], the Fe²⁺-analogue of rhönite, a new mineral from D'Orbigny angrite meteorite. *Mineralogical Magazine*, **80**, 1067–1076.
- Jambon, A. and Boudouma, O. (2011) Evidence for rhönite in angrites D'Orbigny and Sahara 99555 (abstract). *Meteoritics and Planetary Science*, 46 Sup., A113.
- Kuehner, S.M. and Irving, A.J. (2007) Primary ferric-iron-bearing rhönite in plutonic igneous angrite NWA 4590: implications for redox conditions on the angrite parent body. in: *EOS, 88, Fall Meeting Supplement. Abs., P41A-0219*.
- Kunzmann, T. (1989) *Rhönit: Mineralchemie, Paragenese und Stabilität in alkalibasaltischen Vulkaniten, Ein Beitrag zur Mineralogenese der Rhönit Änimagnit-Mischkristallgruppe*. Dissertation Universität München, Germany.
- Kunzmann, T. (1999) The aenigmatite-rhönite mineral group. *European Journal of Mineralogy*, **11**, 743–756.
- Kurat, G., Varela, M.E., Brandstätter, F., Weckwerth, G., Clayton, R., Weber, H.W., Schultz, L., Wäsch, E. and Nazarov M.A. (2004) D'Orbigny: A non-igneous angritic achondrite? *Geochimica et Cosmochimica Acta*, **68**, 1901–1921.
- Lavrent'ev, Yu.G., Karmanov, N.S. and Usova, L.V. (2015) Electron probe microanalysis of minerals: Microanalyzer or scanning electron microscope? *Russian Geology and Geophysics*, **56**, 1154–1161.
- Ma, C., Krot, A.N., Nagashima, K. and Tschauer, O. (2014) Warkite, IMA 2013- 129. CNMNC Newsletter No. 20, June 2014: 552; *Mineralogical Magazine*, **78**, 549–558.
- Ma, C. and Krot, A.N. (2015) Addibischhoffite, IMA 2015-001. CNMNC Newsletter No. 25, June 2015, page 532; *Mineralogical Magazine*, **79**, 529–535.
- Ma, C., Paque, J. and Tschauer, O. (2015) Beckettite, IMA 2015-001. CNMNC Newsletter No. 25, June 2015, page 531; *Mineralogical Magazine*, **79**, 529–535.
- McMillan, P., Putnis, A. and Carpenter, M.A. (1984) A Raman-spectroscopic study of Al-Si ordering in synthetic magnesium cordierite. *Physics and Chemistry of Minerals*, **10**, 256–260.
- Melluso, L., Conticelli, S. and Gennaro, R. (2010) Kirschsteinite in the Capo di Bove melilite leucite lava (cecilite), Alban Hills, Italy. *Mineralogical Magazine*, **74**, 887–902.
- Mittlefehldt, D.W., Killgore, M. and Lee, M.T. (2002) Petrology and geochemistry of D'Orbigny, geochemistry of Sahara 99555, and the origins of angrites. *Meteoritics and Planetary Science*, **37**, 345–369.
- Mukhopadhyay, D.K. and Lindsley, D.H. (1983) Phase relations in the join kirschsteinite (CaFeSiO₄) – fayalite (Fe₂SiO₄). *American Mineralogist*, **68**, 1089–1094.

- Olsson, H.B. (1983) Rhönite from Skåne (Scania), southern Sweden. *Geologiska Föreningens i Stockholm Förhandlingar*, **105**, 299–286.
- Peretyazhko, I.S., Savina, E.A., Karmanov, N.S. and Pavlova, L.A. (2014) Silicate–iron fluid media in rhyolitic magma: data on rhyolites from the Nilginskaya Basin, Central Mongolia. *Petrology*, **22**, 255–292.
- Poon, W.C.K., Putnis, A. and Salje, E. (1990) Structural states of Mg cordierite: IV. Raman spectroscopy and local order parameter behavior. *Journal of Physics: Condensed Matter*, **2**, 6361–6372.
- Richardson, I.G. (2004) Tobermorite/jennite- and tobermorite/calcium hydroxide-based models for the structure of C-S-H: applicability to hardened pastes of tricalcium silicate, β -dicalcium silicate, Portland cement, and blends of Portland cement with blast-furnace slag, metakaolin, or silica fume. *Cement and Concrete Research*, **34**, 1733–1777.
- Schreyer, W., Maresch, W.V., Daniels, P. and Wolfsdorff, P. (1990) Potassic cordierite: characteristic minerals for high-temperature, very low-pressure environments. *Contribution to Mineralogy and Petrology*, **105**, 162–172.
- Sharigin, V.V., Kóthay, K., Szabó, Cs., Timina, T.Ju., Török, K., Vapnik, Ye. and Kuzmin, D.V. (2011) Rhönite in alkali basalts: silicate melt inclusions in olivine phenocrysts. *Russian Geology and Geophysics*, **52**, 1334–1352.
- Sokol, E., Sharygin, V., Kalugin, V., Volkova, N. and Nignatulina, E. (2002) Fayalite and kirschsteinite solid solutions in melts from burned spoil-heaps, South Urals, Russia. *European Journal of Mineralogy*, **14**, 795–807.
- Treiman, A.H. (2008) Rhönite in Luna 24 pyroxenes: First find from the Moon, and implications for volatiles in planetary magmas. *American Mineralogist*, **93**, 488–491.
- Žáček, V., Skála, R. and Zdeněk, D. (2015) Combustion metamorphism in the Most Basin. Pp. 162–202 in: *Coal and Peat Fires: A Global Perspective* (B. Glenn, A. Prakash and E.V. Sokol, editors). Elsevier, New York.